NOTCH-driven oscillations control cell fate decisions during intestinal homeostasis

Sonja D. C. Weterings[1,*], Hiromune Eto[1,*], Jan-Daniël de Leede[1], Amir Giladi[2], Mirjam E. Hoekstra[3], Wouter F. Beijk[3], Esther J. M. Liefting[1], Karen B. van den Anker[1], Jacco van Rheenen[3], Alexander van Oudenaarden[2] and Katharina F. Sonnen[1,#]

[1]Hubrecht Institute-KNAW (Royal Netherlands Academy of Arts and Sciences), University Medical Center Utrecht, Utrecht, The Netherlands

[2]Oncode Institute, Hubrecht Institute-KNAW (Royal Netherlands Academy of Arts and Sciences) and University Medical Center Utrecht, Utrecht, The Netherlands.

[3]Division of Molecular Pathology, Oncode Institute, The Netherlands Cancer Institute, Amsterdam, Netherlands.

*These authors contributed equally.

[#]Correspondence: k.sonnen@hubrecht.eu

Intestinal homeostasis requires tight regulation of stem cell maintenance and commitment to absorptive and secretory cells, two key intestinal lineages[1,2]. While major signalling pathways critical for this control have been identified[3], how they achieve such a tight balance in cell type composition remains unclear. Here, we uncover dynamic expression of Hes1, a direct NOTCH target[3], in intestinal stem and progenitor cells, and investigate its role *in vivo* and *in vitro*. A knock-in reporter[4] reveals distinct, cell-specific period lengths in Hes1 oscillations that form a gradient along the crypt-villus axis. Whereas secretory precursors oscillate at low periods, absorptive precursors oscillate at higher periods before transitioning to a differentiated state. To test the function of different oscillation periods, we innovated a microfluidic system that modulates Hes1 oscillations in organoids. We find that varying the oscillation period modulates secretory cell differentiation: While 90-min oscillations promote Paneth cells, 130-min oscillations increase formation of other secretory subtypes. Moreover, low-period oscillations support stemness and a proliferative state. Our study provides the first clear evidence that information for tissue homeostasis in the intestine is encoded in the temporal dynamics of signalling components.

Main

The intestinal epithelium renews every four to five days, maintaining stem and progenitor cells in the crypt and differentiated cells in the villus[5,6]. Dysregulation of intestinal renewal can result in intestinal atrophy, fibrosis and cancer[7]. Constant renewal and differentiation must therefore occur robustly across the lifespan of an organism. The secretory-to-absorptive cell ratio is crucial for efficient nutrient absorption and digestion, varying along the anteroposterior axis from approximately 1:6 in the small intestine to 1:3 in the large intestine[3,8-10]. Among secretory cells, goblet cells and Paneth cells are the most abundant, comprising 10–15% and 5% of the total epithelial cell population in the small intestine, respectively[11,12]. To maintain this cell-type composition, tissue-wide coordination of cell signalling is fundamental. Indeed, antagonistic gradients of WNT, EGF and NOTCH in the crypt and BMP in the villus determine the general organization of the crypt-villus axis[3]. Within the crypt, NOTCH signalling modulates critical cell fate decisions, including retention of stem cell fate and commitment to secretory or absorptive fate[1,2]. Over-activating NOTCH signalling constantly, such as through the overexpression of NICD (NOTCH intracellular domain), results in the loss of secretory cells and disrupts the vital balance between stem, absorptive and secretory cells[13]. The NOTCH target gene Hes1, which is highly expressed in the crypt, is crucial for these decisions as it represses several important differentiation factors[14,15]. In mice, Hes1 knockout is perinatally lethal due to brain defects; in the gut, it entirely skews the balance of secretory and absorptive cells towards the secretory lineage[14,15].

Such static perturbations have not resolved critical questions about the maintenance of intestinal organisation, including how the intestine balances stem cell maintenance with differentiation, how the correct number of absorptive and secretory cells is specified, and what distinguishes secretory subtypes. Interestingly, NOTCH signalling acts dynamically in several tissues, rather than being “on or off”[16]. Complex dynamics can encode information, for instance, through signal duration or the periodicity of oscillations[17]. Members of the Hes family of transcriptional repressors, which are downstream of NOTCH signalling, have an intrinsic propensity to oscillate due to their own repressive feedback loop[18]. Hes1, for instance, oscillates during vertebrate segmentation and in the nervous system, muscle stem cells and pancreas[18-21]. While Hes1 dynamics have been proposed[22] to occur in the intestine, and recently described

for Hes6 in enteroendocrine precursors[23], the nature and function of these oscillations remains untested *in vivo*. In addition, whether the mere presence or dynamic expression of such factors regulates cellular behaviour remains unclear.

NOTCH-driven Hes1 oscillations occur in the small intestine

To investigate whether NOTCH-signalling dynamics occur in the small intestine, we used a knock-in mouse reporter line. The reporter is integrated into the Hes1 locus, a direct target of NOTCH signalling, to generate the fusion protein Hes1-Achilles (Fig. 1a)[4]. Homozygous Hes1-Achilles reporter mice were viable[4] and showed no signs of intestinal insufficiency (i.e., weight loss or diarrhoea). We found similar cell type distributions within the crypt and villus in homozygous Hes1 reporter mice compared to wild-type mice (Extended Data Fig. 1)[4], indicating that endogenous Hes1 tagging had no effect on intestinal patterning. As expected, Hes1-Achilles expression was restricted to the crypt region[24] (Fig. 1b). It also showed a salt-pepper pattern in the crypt bottom where stem cells reside next to Hes1-negative Paneth cells. However, we observed more variability in Hes1-Achilles expression levels in cells located higher in the crypt. This observation suggested dynamic Hes1 expression in the small intestine.

To visualise Hes1 expression in real-time, we performed intravital imaging on the small intestine of mice expressing the Hes1-Achilles together with a fluorescent nuclear marker (H2B-mCherry). Phototoxicity and significant peristaltic movements of the gut restricted imaging quality and duration. Despite this, we tracked single cells in crypts over three hours and quantified Hes1-Achilles levels over time. We found that Hes1-Achilles was highly dynamic in these crypt cells (Fig. 1c, Supplemental Movie 1). Some cells exhibited rapid increases or decreases in Hes1-Achilles expression, while others displayed more gradual changes in Hes1-Achilles. We also observed cells at the crypt bottom that were constantly low in Hes1-Achilles expression, likely corresponding to Paneth cells (Extended Data Fig. 2). These observations suggest that Hes1 is dynamic in the small intestine *in vivo*.

To quantify these dynamics with higher spatiotemporal resolution, we generated intestinal organoids from the proximal small intestine of mice expressing the Hes1-Achilles together with a fluorescent nuclear marker (H2B-mCherry[25] or iRFPnucmem[4])

(Fig. 1d). Intestinal organoids effectively mimic the cellular composition of the *in vivo* gut, including the differentiation into enterocytes and the two predominant secretory subtypes, Paneth and goblet cells[12]. Hes1-Achilles-expressing organoids showed a gradient of Hes1-Achilles expression, with the highest signal within the crypt, recapitulating the *in vivo* expression pattern[24,26] (Fig. 1b, d).

To confirm a connection between the observed Hes1 dynamics and NOTCH activity, we first performed immunofluorescence (IF) staining against Hes1, which overlapped with reporter expression (Extended Data Fig. 3a). We then inhibited NOTCH signalling using DAPT (N-[N-(3, 5-difluorophenacetyl)-l-alanyl]-s-phenylglycinet-butyl ester), a small molecule gamma-secretase inhibitor. This treatment led to a drop in Hes1-Achilles levels within 30 min (Extended Data Fig. 3b, c), confirming that Hes1-Achilles expression is dependent on NOTCH signalling.

We live-imaged Hes1-Achilles organoids using an inverted light-sheet microscope, which allows high-resolution imaging for single-cell tracking with low phototoxicity. Hes1-Achilles was highly dynamic in most crypt cells by visual inspection (Fig. 1d, Supplemental Movie 2). Given that NOTCH signalling is known to cause spatial synchronization[27], we examined crypt dynamics in addition to single-cell dynamics. When quantifying Hes1-Achilles dynamics in whole crypts, we observed varying expression levels over time (Fig. 1e). Kymographs generated along the crypt-villus axis indicated local, synchronized dynamics rather than the clear waves observed during somitogenesis[28] (Fig. 1f). Subsequently, we quantified Hes1-Achilles expression in single cells, focusing on the crypt region. We divided cell positions into bottom and side regions to account for broad differences in cell-type composition (Fig. 1g). Single-cell tracks revealed that Hes1-Achilles expression displayed a variety of dynamics, oscillating in many cells in the bottom and side regions of the crypt (Fig. 1g and Extended Data Fig. 4). To quantify these oscillations, we used wavelet analysis, which fits wavelets of finite length centred around each time point along the track, providing an idea of “instant” oscillatory dynamics[29]. We determined the mean intensity, amplitude and the period of the detected oscillations (Fig. 1h). We did not observe differences in intensity or oscillation amplitude between bottom and side cells (Fig. 1i, j). Period quantifications revealed a broad range of periodicities between 75 and 200 min, with 3 main peaks at approximately 90, 130 and 170 min (Fig. 1k,

Extended Data Fig. 4, 5). Thus, Hes1 expression oscillates with a range of periods in the crypts of intestinal organoids.

Single-cell tracking in 2D organoids characterizes Hes1 oscillations

To fully capture the heterogeneity of Hes1 dynamics, we turned to a 2D organoid system (Fig. 2a). These simplified *in vitro* models are derived from intestinal stem cells or crypts and grow as a monolayer on a hydrogel-coated flat surface[30]. Due to its planar geometry, this system offers more straightforward automatic image analysis for single-cell tracking than the 3D organoid model, allowing higher-throughput quantification. The tissue self-organized into near-radially symmetric crypt-villus structures as seen in previous literature[31,32]. Verification with immunostaining confirmed that our system recapitulated differentiation into key cell types observed *in vivo* and in 3D organoid cultures, such as stem cells (Olfm4$^+$), Paneth cells (Lyz1$^+$), secretory cells (WGA$^+$) and enterocytes (AldoB$^+$) (Extended Data Fig. 6). Comparisons of these markers with Hes1-Achilles expression confirmed the absence of Hes1-Achilles in Paneth and secretory cells and high expression in stem cells. We observed graded Hes1-Achilles expression down the crypt-villus axis, correlating very well with the proliferation markers Sox9 and Ki67, extending to the TA (transit amplifying) zone[33]. Consistent with the literature[24], Hes1-Achilles expression was absent in enterocytes (Fig. 2a, 1b).

We conducted 24-hour live-imaging at high spatial resolution to capture Hes1-Achilles dynamics in individual cells (Fig. 2a, Supplemental Movie 3). For high-throughput analysis, we developed an automatic nuclear segmentation and tracking pipeline to quantify Hes1-Achilles signals in individual cells (Fig. 2a, Supplemental Movies 4 and 5, see Methods for details). Given that Hes1 displays 1.5 – 3 h period oscillations in other systems[34], we excluded tracks shorter than 8 hours. This approach therefore quantifies *ultradian* oscillations, i.e., with periodicity occurring from one to several hours, with sufficient confidence. This filtering resulted in a complete track length distribution of 8–20 hours (Extended Data Fig. 7a, b).

The analysis of single-cell tracks revealed a diverse range of Hes1-Achilles dynamics, characterized by varying intensity levels over time. We applied Fourier transformation to the intensity traces to identify frequency peaks characteristic of oscillatory systems.

After removing contributions resulting from fundamental and harmonic frequencies related to track lengths (see Methods), the mean Fourier spectrum across all tracks unveiled a broad but distinct peak in the 75-250 min range (Fig. 2b). In addition to short intensity fluctuations and long-term increases or decreases in Hes1-Achilles levels, most cells exhibited oscillatory behaviour with distinct periodicity (Fig. 2b,c). These oscillations show similar periodicity to other systems where dynamic expression plays a critical coordinating role[34]. These data reveal that Hes1 expression shows ultradian oscillatory behaviour in the small intestine.

Synchronisation of Hes1 oscillations

To analyse intercellular synchronization in more detail, we generated kymographs along lines from crypt centres towards villi, which revealed various neighbouring vertical lines of Hes1-Achilles expression along space, supporting the presence of tissue-wide coordination (Fig. 2d, Extended Data Fig. 8a). To quantify local synchrony of Hes1-Achilles oscillations between neighbouring cells, we calculated the Kuramoto order parameter between a cell and its direct neighbours (Extended Data Fig. 8b, c). The median order parameter across the tissue was 0.39 for all tracks, which indicates the oscillations of neighbouring cells are not always synchronized, explaining why such periodicity has been difficult to observe *in vivo*. However, we occasionally observed spikes in the instantaneous order parameter, reaching values near 1. These transient increases in synchrony also appeared as sporadic patches in the live imaging data (Extended Data Fig. 8c, Supplemental Movie 6).

Interestingly, we noticed Hes1-Achilles expression peaks in daughter cells after division (Supplemental Movie 7, Extended Data Fig. 8d, e). We observed a significant dip in Hes1-Achilles expression at mitosis, likely due to nuclear envelope breakdown and the subsequent release of Hes1-Achilles into the cytosol. Examining the phase of Hes1-Achilles oscillations around cell division, we found that phases synchronised approximately 1.5 to 1 hour before mitosis and were maintained until about 1 to 1.5 hours after division (Extended Data Fig. 8f, g). These findings suggest correlation between cell division and the synchronous Hes1 behaviour of neighbouring cells.

205 ***Backtracking reveals a period gradient along the crypt-villus axis***

206 To elucidate the spatial distribution of oscillatory Hes1 behaviours in the intestine, we
207 developed an analysis framework to define the crypt centre in our live imaging data.
208 By backtracking from immunofluorescence staining of cell type markers, we defined
209 stem, Paneth and secretory cells (Fig. 2e,f, see Methods). We then calculated the
210 distance from the crypt centre as the number of cells away from Paneth cells (Fig. 2g,
211 Extended Data Fig. 9a).

212 Quantifying Hes1-Achilles dynamics within this framework, we observed that the
213 gradient of Hes1-Achilles intensity decreased with distance from Paneth cells[24] (Fig.
214 2h), supporting the validity of our approach. Wavelet analysis revealed an amplitude
215 gradient correlating well with the intensity gradient (Fig. 2i, Extended Data Fig. 9b).
216 The wavelet power spectra for individual tracks showed varied oscillatory patterns:
217 some tracks oscillated at a single period (Extended Data Fig. 10a), while others
218 exhibited changes in period or had multiple, nested periods (Extended Data Fig. 10b,
219 c), indicating complex oscillatory behaviour.

220 The distribution of periods changed significantly with increasing cell distance from
221 Paneth cells (Extended Data Fig. 9c). Notably, lower periods existed almost
222 exclusively near Paneth cells (Fig. 2j). Periods less than 80 min and those between
223 80-100 min peaked at around 12 μm (approximately one cell distance from Paneth
224 cells) and had a median around 22-25 μm (within two cells). This conclusion agrees
225 with periodicity quantified in the crypts of 3D organoids (Fig. 1k): Cells near Paneth
226 cells had a prominent peak at 90 min but showed a broader distribution extending
227 further up the crypt-villus axis. Thus, a period gradient was detectable, with periods
228 lengthening as the distance from Paneth cells increased.

229

230 ***Cell type inference reveals cell type-specific Hes1 dynamics***

231 To determine which cells exhibited specific oscillatory behaviour, we defined cell types
232 based on IF staining after live imaging. In addition to stem, secretory and Paneth cells
233 (Fig. 2e, f), we classified immature progenitor cells (IMPCs, precursors to secretory
234 cells), enterocytes and TA cells (Fig. 3a, b, further details in methods). To distinguish
235 the TA cell states more clearly, i.e., more progenitor-like or more differentiated, we

236 subdivided them into Early (up to three cells) and Late TA cells (from four cells
237 onwards) based on their positions relative to Paneth cells (Fig. 3a, b, further details in
238 methods). Based on this cell type classification, we reanalysed our tracks. Different
239 cell types were positionally distributed, as expected, according to their distance from
240 Paneth cells: stem cells were mostly at the 1-cell position, and enterocytes were
241 further away (>6 cells) (Extended Data Fig. 11a). Hes1-Achilles expression was
242 highest in stem cells and followed a gradient that decreased from Early to Late TA cells
243 and then to enterocytes, while secretory cells showed low Hes1-Achilles expression
244 (Fig. 3c, Extended Data Fig. 11b-e).

245 Next, we re-evaluated our wavelet analysis and detected significant differences in
246 oscillation period between cell types (Fig. 3d). Stem cells and Early TA cells had lower
247 medians (132 min for both) compared to Late TA (142min) and enterocytes (149min).
248 The latter included cells transitioning from TA cells to enterocytes during live imaging
249 and showed a prominent peak at 170 min period. This is consistent with the period
250 gradient observed earlier. Amplitudes also correlated well with intensity (Extended
251 Data Fig. 11f). IMPCs had a median at 133 min, similar to stem or Early TA cells, and
252 also a distinct peak at around 90 min (Fig. 3d).

253 To investigate cells transitioning to the absorptive or secretory lineage in detail, we
254 focused on cells showing a Hes1-Achilles expression arrest midway through the tracks
255 (Fig. 3e-i). Most progenitor-to-enterocyte transitions occurred far down the crypt-villus
256 "differentiation" gradient (Fig. 3e, g, h, Supplemental Movie 8). This gradient indicates
257 that cells gradually decreased in Hes1-Achilles intensity and transitioned to a low-
258 Hes1-Achilles, differentiated state as they moved away from the crypt centre. In the
259 second case, most IMPC transitions occurred very early in the crypt-villus axis[35],
260 peaking at the 2-cell position, with some even occurring directly adjacent to Paneth
261 cells (Fig. 3f, g, ii, Supplemental Movie 9). Most cells in this vicinity were Hes1-
262 Achilles-high cells (Fig. 2h, Extended Data Fig. 11a-e). These cells therefore
263 transitioned early from a high-expression oscillatory state to a Hes1-Achilles-low state,
264 committing to the secretory lineage.

265 When analysing the cell-type dependence of local synchronization, we found that
266 Kuramoto order parameters between cells of each cell type and their neighbours were
267 comparable with a slight trend to higher values for transitioning enterocytes (Extended

Data Fig. 11g). Finally, we quantified cell cycle length for each proliferating cell type (Extended Data Fig. 11h). Stem and TA cells cycled on average approximately every 11 h[35], while IMPCs had long cycling times of 18.3 h. When aligning tracks to the point of cell division, all cell types showed a dip in Hes1-Achilles expression at division followed by a peak (Extended Data Fig. 11i). Even though IMPCs were mostly Hes1-Achilles low throughout their lifetime (Extended Data Fig. 11e), they still divided once more after a drop in Hes1-Achilles signal to give rise to secretory cells.

Thus, our data suggest that stem and progenitor cells show lower-period Hes1 oscillations. Moreover, cells commit to a secretory fate in the low-period region of the Hes1 oscillation gradient, where IMPCs oscillate with low and mid-range periods before transitioning. Conversely, enterocyte precursors oscillate at higher periods before transitioning in the high-period region of the Hes1 gradient.

Modulation of NOTCH signalling dynamics

Next, we sought to modulate dynamics, rather than absolute expression levels, to determine the functional effects of different oscillation periods. To this end, we established a microfluidic system for the on-chip culture of 3D organoids (Fig. 4a, Extended Data Fig. 12a-c). This system allows modulation of culture conditions over time whilst simultaneously monitoring Hes1-Achilles dynamics by fluorescence microscopy. Marker expression for stem cells (LGR5-DTR-GFP[36]), enterocytes (CK20) and apoptosis (cleaved Caspase-3) verified proper organoid differentiation and survival in the microfluidic system (Extended Data Fig. 12d,e).

To control oscillations, we used an entrainment approach, which synchronises endogenous oscillations with periodic external pulses (Fig. 4a)[36-38]. We achieved synchronisation of Hes1-Achilles oscillations through periodic application of DAPT[38,39]. We aimed at modulating oscillations to 90, 130 and 170 min, spanning the range of the Hes1-Achilles period gradient we had detected earlier. We selected a DAPT concentration that provided only partial inhibition of Hes1-Achilles when applied continuously to subtly modulated signalling activity (Extended Data Fig. 12f). Furthermore, we initially adjusted DAPT concentrations according to each period — 90 min, 130 min, and 170 min — to ensure the cumulative dose remained consistent across all conditions. To monitor drug pulses, we tracked the flow of DMSO or DAPT

into the microfluidic chamber using the fluorescent dye cascade blue (Extended Data Fig. 12g, h). We then analysed Hes1-Achilles dynamics by quantifying reporter expression within crypts (Fig. 4a).

Periodic DAPT pulses synchronised endogenous Hes1-Achilles oscillations with the external DAPT rhythm across all entrainment periods (Fig. 4b-g, Supplemental Movie 10). We quantified the amplitude and fold-change of absolute Hes1-Achilles levels to ensure there were only changes in Hes1-Achilles-oscillation period. While 90- and 130-min pulses did not alter amplitude or absolute Hes1-Achilles levels, significant changes in amplitude were observed with 170-min pulses (Extended Data Fig. 12i-k). Therefore, we lowered the DAPT concentration to promote 170-min entrainment conditions, resulting in entrainment without altering amplitude or absolute Hes1-Achilles levels (Fig. 4h, i). Thus, our microfluidic system effectively modulates the period of NOTCH-driven oscillations in intestinal organoids (Fig. 4j).

Bulk RNAseq indicates changes in cell type composition upon modulation of oscillations

To identify potential subtle changes in cell type composition upon modulation of Notch-driven oscillations, we performed bulk RNA sequencing (bulk RNAseq) after entraining oscillations to 3 different periods (90-, 130- and 170-min) for 3 different durations (24-, 48- and 72-hours) (Fig. 5a). Organoids were harvested at the same 'developmental age' (i.e., 4 days after passaging) to reduce potential variations in cell type composition based on organoid age (Extended Data Fig. 13a, b). We compared results based on the duration of on-chip culture to remove any bias, i.e., we for instance compared all 24 h DAPT samples to a 24 h DMSO control.

When investigating expression of known cell type markers, we indeed found subtle effects depending on entrainment conditions (Extended Data Fig. 14). Both 130- and 170-min entrainment generally showed similar expression changes. There was an increase in Paneth cell markers after 72 h of 90-min entrainment (90min(72h)-entrainment) as well as a slight decrease in enterocyte markers after 130min(72h)-entrainment. In the latter condition, we also found an increase in markers for fetal-like stem cells. Fetal-like stem cells (markers *Msln, Ly6a, Clu, Anax1*) are found in the gut

during embryonic development[40], regeneration of adult intestines[41], in organoids after passaging[42] and occasionally in the *in vivo* small intestine (Extended Data Fig. 13).

To more accurately extract information on cell type composition, we applied the Latent Dirichlet Allocation (LDA) approach to our bulk RNAseq data, using the single-cell RNAseq (scRNAseq) data presented in Bues et al. (2022)[40] (Extended Data Fig. 15). Our approach performs deconvolution of bulk RNAseq data into distinct cellular states[40]. Cell-type changes between entrainment periods and controls (Extended Data Fig. 15e-n) revealed an over-representation of Paneth cells after 90min(72h)-entrainment. For 130min(72h)-entrainment, we observed a decrease in enterocytes and an increase in progenitor cells, including fetal-like stem cells. In addition, there were indications of a decrease in enteroendocrine cells after 170min(72h)-entrainment, even though expression of enteroendocrine markers was low, potentially leading to large variations in observed results (Extended Data Fig. 15e-g, j). Thus, we found indications for changes in stem cell maintenance and differentiation depending on oscillation period.

NOTCH-driven oscillations modulate crypt maintenance

To confirm whether oscillation period regulates cell type composition, we quantified cell types by staining for cell type markers using IF upon entrainment. We focused on conditions with the most potent effects, as indicated by bulk RNAseq data (24 h: 90 and 130 min; 72 h: 90, 130 and 170 min) (Fig. 5a). WT or Lgr5-DTR-GFP organoids[43] were entrained, then stained for WGA (secretory cells), LYZ1 (Paneth cells), SOX9 (progenitor zone) and SCA-1 (fetal-like stem cells). To quantify changes in cell type abundance after entrainment from a large number of images, we performed superpixel analysis (Extended Data Fig. 16a). To ensure the accuracy of our study on homeostatic organoids, we excluded small, non-budded organoids from our analysis.

As a control for our microfluidics experiments, we continuously treated organoids with the average DAPT concentration equivalent to the cumulative dose of microfluidics experiments (0.48 μM for 90- and 130min entrainment, while in 170-min entrainment only 0.35 μM was used). This treatment resulted in no changes in morphology or cell type distribution (Extended Data Fig. 17), supporting the conclusion that any observed

362 effects upon entrainment were due to changes in oscillation periods rather than
363 absolute NOTCH signalling levels.

364 Whereas entrainment for 24 h showed no apparent changes in cell type composition,
365 presumably due to the required time for differentiation and marker expression
366 (Extended Data Fig. 16b-g), we determined two main effects after 72 h of entrainment.

367 First, 90min(72h)- and 130min(72h)-entrainment increased the relative amount of
368 LGR5$^+$ stem and SOX9+ progenitor cells in organoids, while 170min(72h)-entrainment
369 did not (Fig. 6b,c, Extended Data Fig. 16h). Corresponding to a shift towards
370 undifferentiated crypt cells, organoids contained fewer enterocytes (determined as
371 LGR5-, SOX9- and WGA- superpixels) (Extended Data Fig. 16i, j). In contrast to the
372 bulk RNAseq data, we could not confirm a significant effect on fetal-like stem cells,
373 even though we found a trend towards higher percentages of SCA-1$^+$ cells under all
374 entrainment conditions (Extended Data Fig. 16k). Thus, our data suggest that low (90-
375 to 130-min) period oscillations shift the organoid cell balance towards undifferentiated
376 stem and progenitor cells.

377 Second, we identified a period-specific effect on the number of secretory cells.
378 Consistent with the bulk RNAseq data, we found that 90min(72h)-entrainment
379 increased the percentage of LYZ1$^+$ Paneth cells (Fig. 5d, e). In contrast, no changes
380 in the percentage of Paneth cells were detected in other entrainment periods (Fig. 5d).
381 When analysing the broader secretory lineage marker WGA, we found an increase in
382 WGA$^+$ cells specifically in the 130min(72h)-entrainment. 90min(72h)-entrainment
383 showed a trend towards higher percentages ($p = 0.052$), which is consistent with the
384 increased percentage in Paneth cells as one of the secretory subtypes (Fig. 5f,g, see
385 above). Conversely, 170min(72h)-entrainment did not affect this percentage. This
386 suggests that 90-min oscillations promote Paneth cell differentiation, while 130-min
387 oscillations promote differentiation of secretory cells other than Paneth cells.

388

389 **Discussion**

390 Here, we find that Hes1, a direct target of NOTCH signalling, oscillates in the intestine
391 with the periodicity of 90 min at the crypt bottom and 170 min towards the villi.
392 Modulation of the oscillation period using microfluidics-based perturbation resulted in

393 significant changes in cell type composition (Fig. 5h). While our microfluidic approach
394 targets entire 3D organoids, which leads to an increase in synchronization of
395 oscillations between neighbouring cells for all entrainment conditions, we identified
396 period-specific effects. This highlights that (1) it is not intercellular synchronization that
397 modulates cell type composition and (2) specific periods promote specific changes in
398 cell identity.

399 While enterocyte precursors slow down in Hes1 oscillations towards high periods,
400 secretory precursors show low- and mid-range-period oscillations before transitioning.
401 We show that entraining oscillations to 90-min periods promotes Paneth cell formation,
402 while 130-min oscillations support the appearance of secretory cells other than Paneth
403 cells, presumably goblet cells. The period distribution of secretory precursors with few
404 cells oscillating at 90 min and a majority at 130 min is consistent with differences in
405 Paneth (5 %) and goblet cell (10 – 15 %) numbers in the small intestine. This indicates
406 that dynamics play a role in regulating intestinal cell type composition, in particular by
407 modulating secretory cell differentiation. In enteroendocrine progenitors, another
408 secretory subtype, oscillations in the Hes6-target gene Ascl1 have recently been
409 observed, indicating potential oscillations of other Hes genes in the intestine[23]. Since
410 we used a general NOTCH pathway inhibitor to entrain oscillations, our microfluidic
411 system modulates all NOTCH-dependent target genes. Our approach therefore
412 provides unprecedented insight into the functional effects of periodic NOTCH-pathway
413 activity in the intestine. How individual Hes genes contribute to differentiation and
414 interact with Hes1, and its target genes (Atoh1, Ascl1) are interesting directions for
415 future research.

416 Enterocyte precursors have been shown to proliferate more often than secretory
417 precursors before terminally differentiating, which is thought to regulate intestinal
418 enterocyte abundance[35]. We find that enterocyte precursors continue oscillating in
419 Hes1 throughout the crypt, with increasing oscillation periods towards the crypt top.
420 Interestingly, entraining oscillations to periods of 90 and 130 min, but not 170 min,
421 promotes stemness and a proliferative state. This indicates that low-period oscillations
422 prevent enterocyte differentiation in the bottom of the crypt. This agrees with similar
423 findings in other contexts, such as cells in brain and breast tissue, where Hes
424 oscillations correlate with proliferation[44-46]. Our data suggest that it is not the presence
425 of oscillatory factors *per se,* but specific oscillation periods that regulate the number of

426 proliferative cells in the gut. Moreover, we show that Hes1 oscillations are correlated
427 with cell cycle dynamics, with cells consistently showing a peak of Hes1 expression
428 after cell division. Future studies should reveal whether NOTCH-driven oscillations are
429 functionally linked with cell proliferation[47] or indirectly modulate a proliferative state by
430 promoting stemness.

431 Our findings are consistent with a model in which oscillations in the crypt modulate
432 intestinal patterning (Fig. 5h). In this framework, a gradient of periodicity along the
433 crypt-villus axis maintains stemness and a proliferative state towards the bottom of the
434 crypt. This way, enterocyte precursors are maintained in an undifferentiated state
435 throughout the crypt length to expand in cell numbers. Moreover, stem cells
436 differentiate towards secretory cells at the crypt bottom with a 90-min oscillation period
437 promoting Paneth cell formation and 130-min promoting goblet cell formation.

438 These results will drive further investigations into how oscillations are regulated at the
439 cellular level and how oscillations interact with other signalling pathways, including
440 morphogen gradients[48] and intestinal ERK dynamics[49,50], to modulate intestinal cell
441 type composition along the anteroposterior axis of the intestine[10]. This also has direct
442 implications for understanding homeostasis of other tissue types and non-
443 physiological conditions such as inflammation, regeneration and cancer.

444

445

446

447

Figure legends

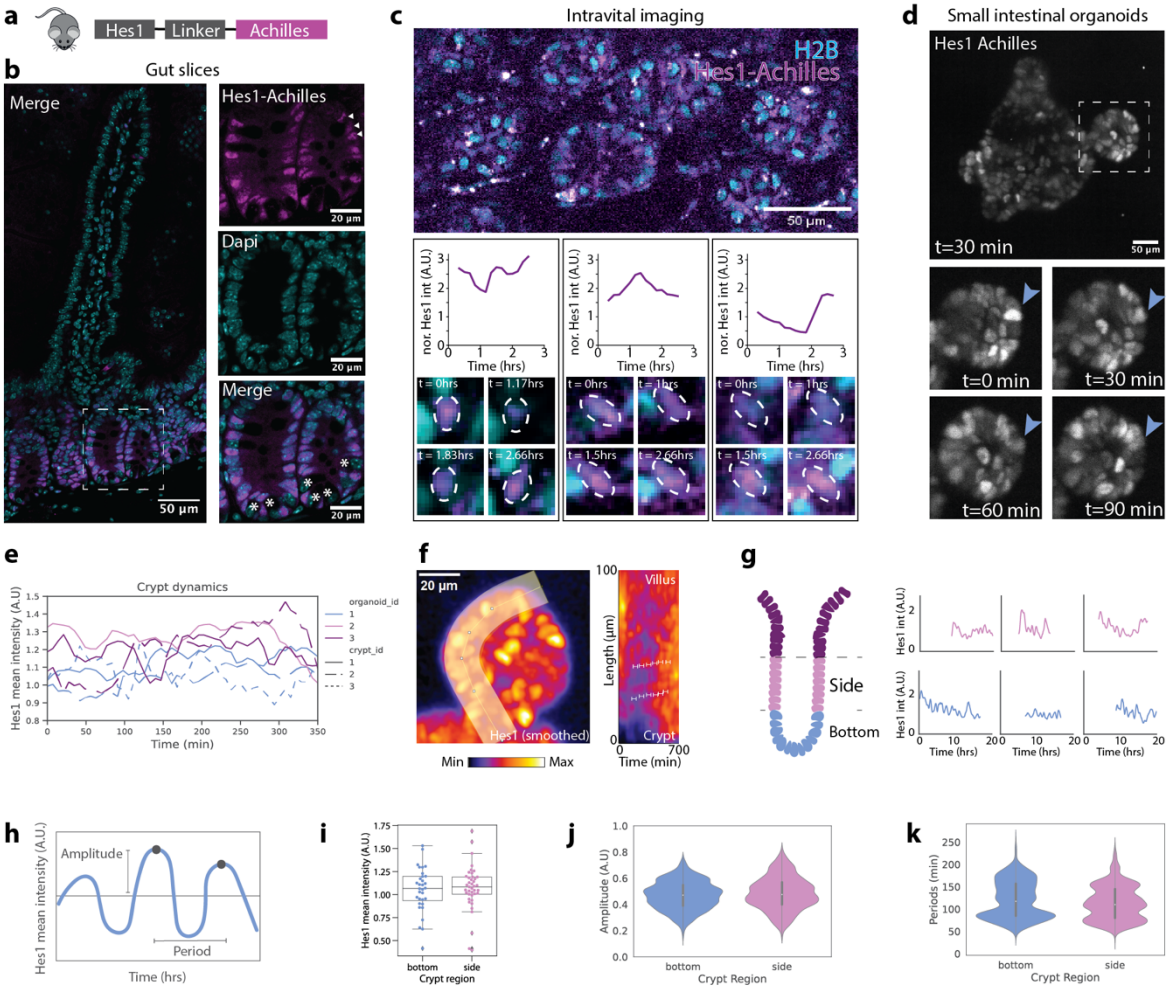

Fig. 1. Hes1 is dynamic in small intestinal homeostasis. (a) Representation of the Hes1-Achilles reporter mouse line. (b) Representative image of Hes1-Achilles gut-slices counterstained with DAPI with magnification to show the crypt (right panels). Hes1-Achilles negative Paneth cells are indicated by asterisks. Arrowheads indicate varying Hes1-Achilles intensity at crypt sides. (c) Intravital imaging of the small intestine, representative image of Hes1-Achilles crossed with H2B-mCherry. Three example single-cell tracks (H2B normalized) are shown with a zoom-in of the associated imaging of these tracks over time. (d) Representative image of a Hes1-Achilles small intestinal organoid and (below) magnifications of crypt over time. Arrows highlight the same cell and its variable expression over time. (e) Hes1-Achilles intensity (mean-normalized) was measured in organoid crypts over time. (f) Kymographs from the crypt to the villus of cultured Hes1-Achilles small intestinal organoids were generated. Left panel: Zoom in of crypt with indicated kymograph line.

Right panel: Kymograph over period of 10 hours and a length of 100µm Scalebar = 50µm (g) Left panel*:* Schematic representation of an organoid bud with bottom (blue) and side (pink) region highlighted. *Right panel:* Representative timeseries data of single-cell tracks in the three regions of the crypt, indicated with colour. (h) Schematic representation of an oscillation, amplitude and period indicated. (i) Quantification of Hes1-Achilles mean intensity. (j, k) Quantification of instantaneous amplitude (j) and period (k) by wavelet transform. Side: n=41 cells; bottom: n=32 cells. Tracks shorter than 7h were excluded.

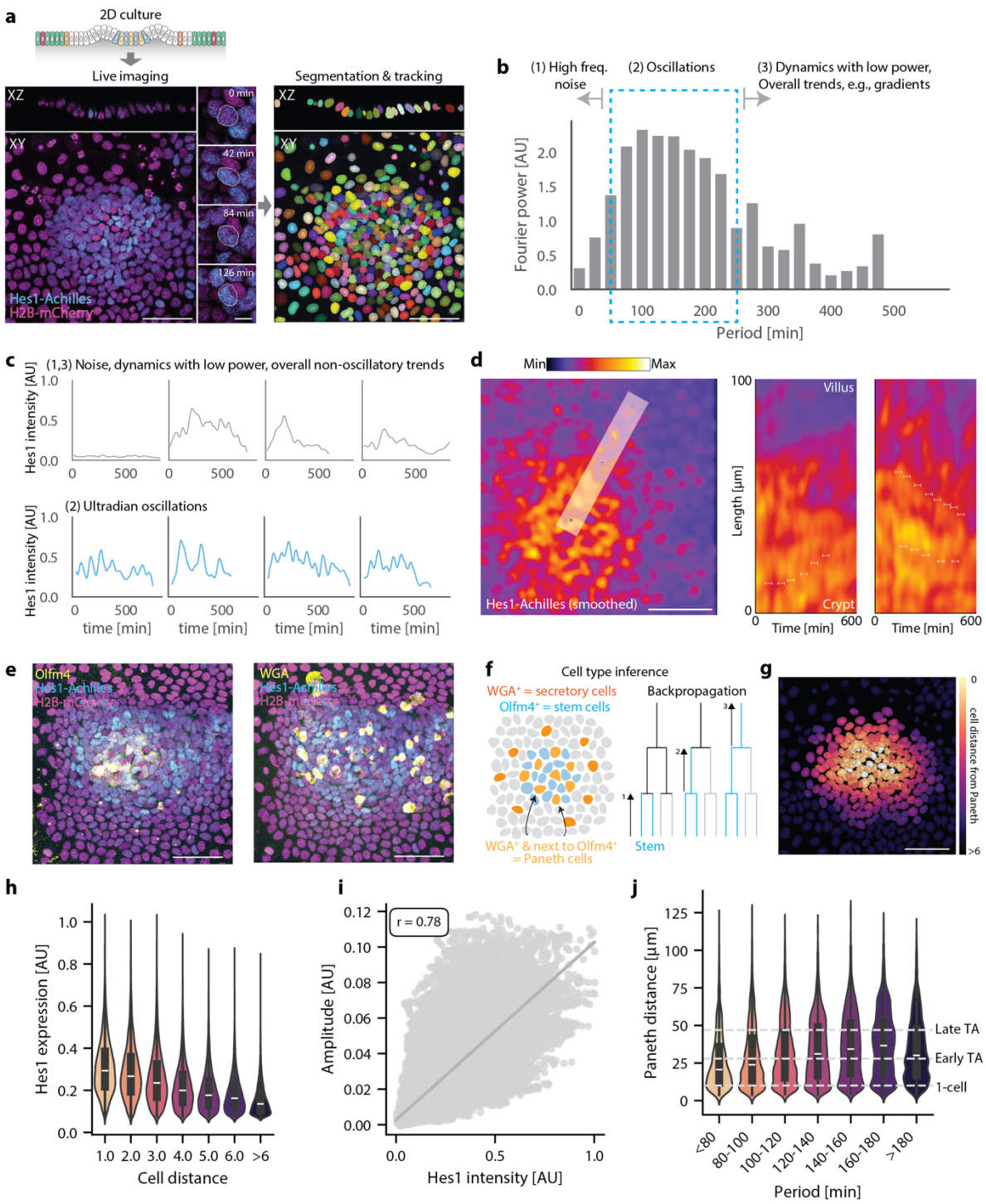

Fig. 2. Single-cell tracking analysis of 2D intestinal organoids reveals an oscillation period gradient along the crypt-villus axis. Intestinal organoids expressing Hes1-Achilles and H2B-mCherry were cultured in 2D, followed by live-imaging and analysis. (a) Schematic representation, snapshots of live-imaging and segmentation result. Scale bars: 50 µm (overall), 5 µm (zoomed-in). (b) Mean Fourier spectrum of single-cell Hes1-Achilles intensity traces after removing fundamental and

479 harmonic frequencies (full spectrum in Extended Data Fig. 7c). (c) Examples of Hes1-
480 Achilles intensity traces over time, with raw data smoothed using a rolling mean over
481 3 timepoints. (d, left) Representative snapshot of a gaussian-smoothed 2D organoid
482 expressing Hes1-Achilles, with a line along a crypt-villus axis from which kymograph
483 was taken. Scale bar: 50 μm. (d, right) Two representative kymographs, brackets
484 showing apparent synchrony (further examples in Extended Data Fig. 8a). (e)
485 Immunofluorescence staining at the end of live imaging for Olfm4 (stem cell) and WGA
486 (secretory cell). Scale bar: 50 μm. (f) Schematic representation of cell type inference
487 to define secretory, stem and Paneth cells. (g) Segmented nuclei representing
488 distance from Paneth cells, scale bar 50 μm. (h) Violin plot of Hes1-Achilles expression
489 vs cell distance from Paneth cells. (i) Scatter plot of amplitude vs Hes1-Achilles
490 intensity from wavelet analysis, with Pearson correlation coefficient, r, calculated by
491 linear least-squares regression, $p = 0.0$. (j) Violin plot of distance from Paneth cells vs
492 period from wavelet analysis. For panels (h, j) n=1901 tracks, N=3 biological
493 replicates, n_{inst} = 147959 instantaneous measurements. Normal distribution was
494 assessed by Shapiro Wilk test, $p<0.05$ for all datasets. Significance was tested by
495 Mann-Whitney U test, with all conditions statistically different from each other, $p<0.05$.

496

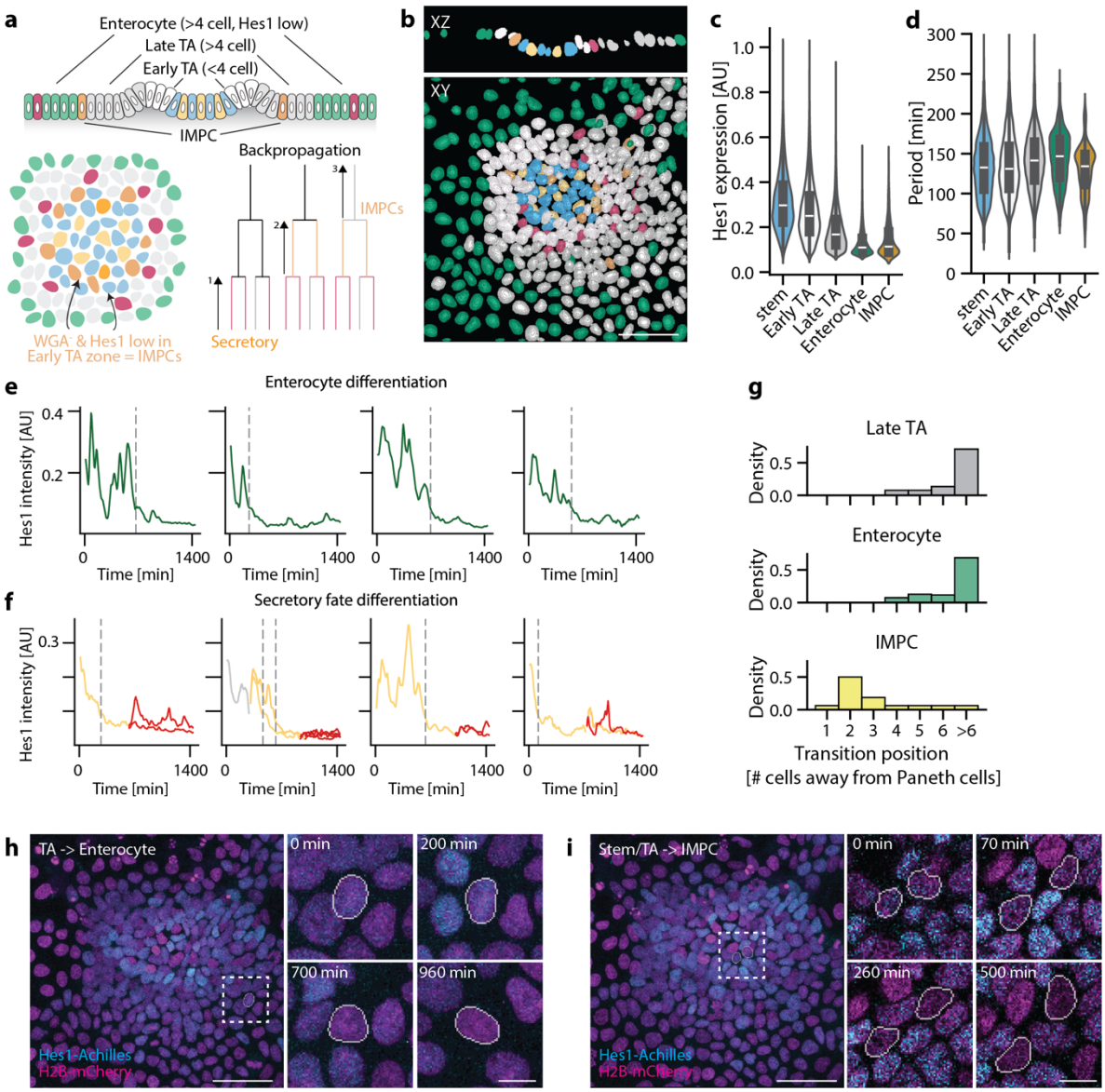

Fig. 3. Different intestinal cell types display distinct Hes1 dynamics. Intestinal cell types were defined for all single-cell tracks from 2D organoid live imaging, followed by analysis. (a) Schematic representation of cell-type inference and (b) segmentation showing resultant classification. Scale bar: 50 µm. (c) Violin plot of Hes1-Achilles expression vs cell type. (d) Violin plot of Hes1-Achilles expression vs period from wavelet analysis. For panels (c, d), n=1901 tracks, N=3 biological replicates, n_{inst} = 147959 instantaneous measurements. Normal distribution was assessed by Shapiro Wilk test, $p<0.05$ for all datasets. Significance was tested by Mann-Whitney U test, with all other cell types compared against stem cells. All comparisons were statistically significant, $p<0.05$. Representative Hes1-Achilles intensity traces for (e) enterocyte differentiation and (f) secretory fate differentiation, grey dotted lines indicating moment

509 of transition (see Methods). (g) Histogram of Hes1-Achilles high-to-low transition
510 position per cell type, $n_{enterocyte}$ = 190, $n_{Late\ TA}$ = 243, n_{IMPC} = 16. Representative images
511 and snapshots of (h) enterocyte differentiation, and (i) secretory cell differentiation in
512 2D organoids expressing Hes1-Achilles and H2B-mCherry. Scale bars: 50 μm
513 (overall), 5 μm (zoomed-in).

514

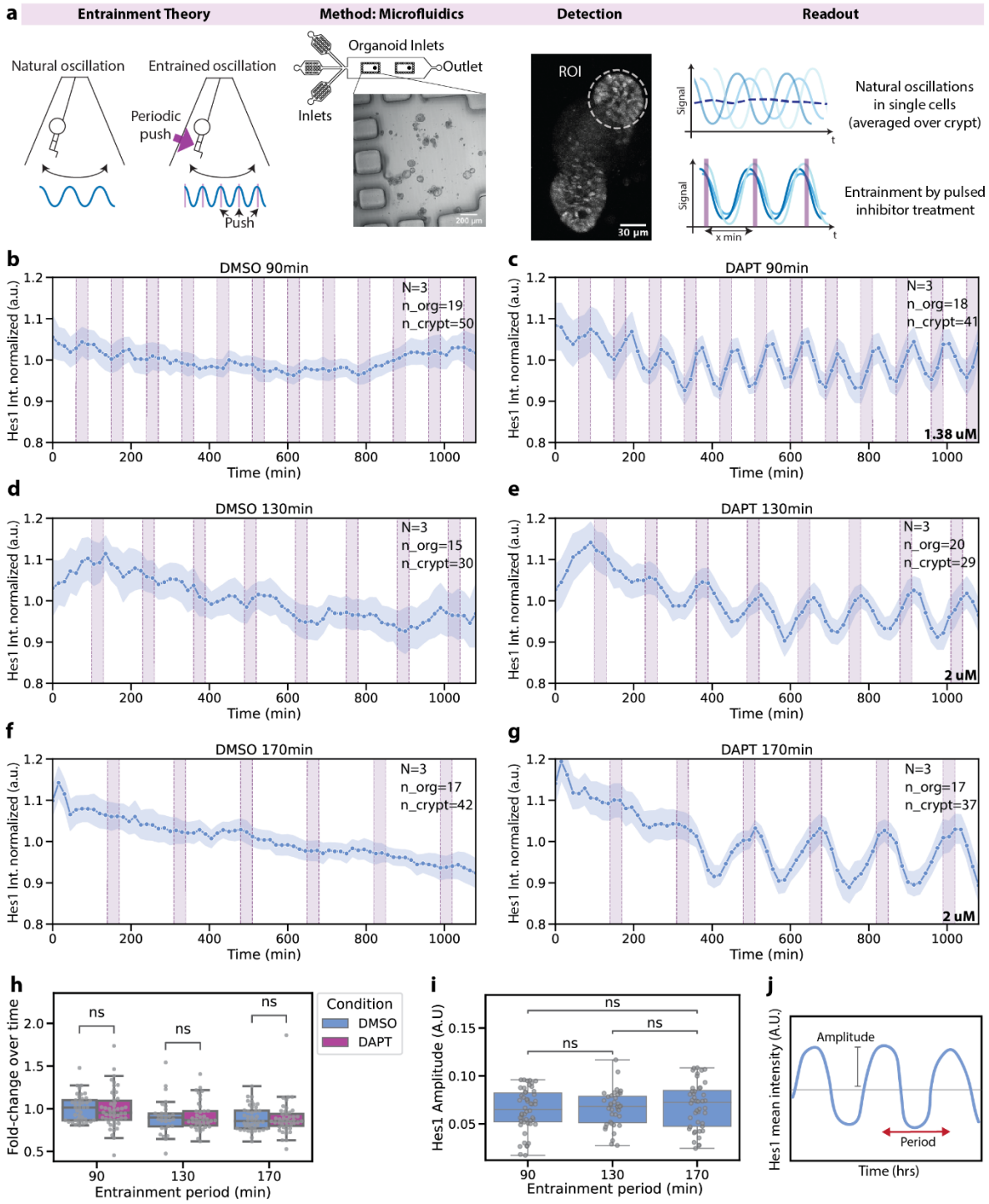

Fig. 4. Entrainment using microfluidics modulates signalling dynamics in organoids. (a) Schematic overview including the entrainment theory, the microfluidic chip, including a representation of organoids cultured within the chip, crypt dynamic detection of Hes1-Achilles intensity overtime and our hypothesis of the experimental read-out Organoids were entrained to a 90- 130- or 170-min period for 20-24 hours. (b-g) Entrainment of Hes1-Achilles oscillations to periodic pulses, 90-(b, c) 130- (d, e)

522 and 170-min (f, g) of the NOTCH inhibitor DAPT (concentration indicated).
523 Quantification of (normalized) Hes1-Achilles signal in organoid crypts. Experiments (N
524 = independent experiments, n_org = individual organoids, n_crypt = individual crypts)
525 were combined using the external force (pink bars) as an objective time reference. (h)
526 Quantification of Hes1-Achilles absolute intensity overtime by calculating the fold-
527 change over time, comparing the intensity of the first 20 timepoints to the last 20
528 timepoints of each condition. Comparison between control (DMSO) and entrainment
529 (DAPT) Hes1-Achilles fold change overtime. Independent t-test was performed per
530 condition. (i) Quantification of amplitude by wavelet transform and comparison
531 between entrainment periods. Mann-Whitney U was performed, with Bonferroni
532 multiple sample correction. (j) Schematic representation of a Hes1 oscillation
533 highlighting the period, which was the only feature changed in experiments shown this
534 Figure.

535

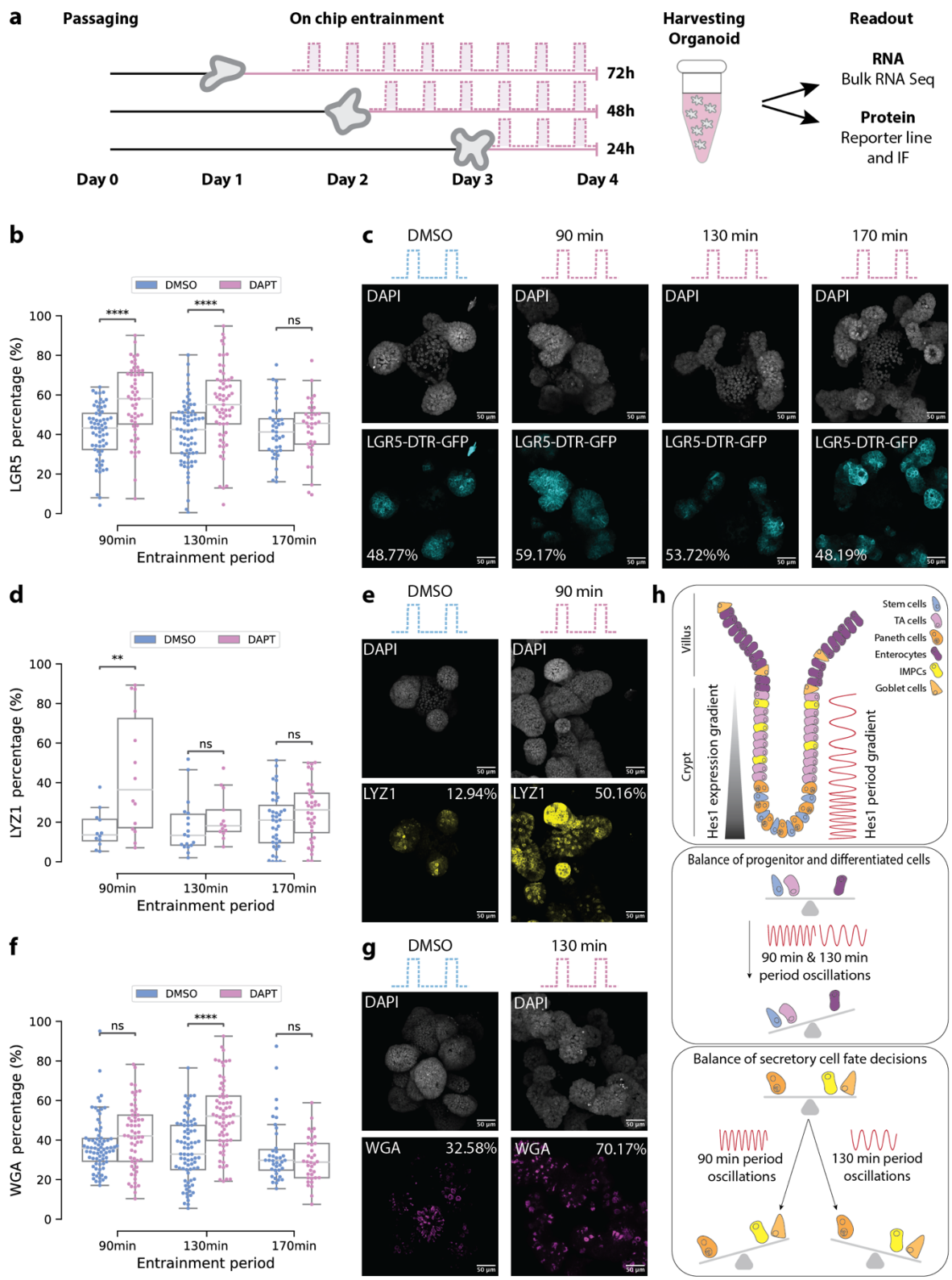

536

537 **Fig. 5. NOTCH signalling dynamics drive crypt maintenance.** (a) Schematic
538 representation of experimental design. Organoids were cultured for one, two or three
539 days in a normal culture dish and entrained within the microfluidic chip for 72, 48 or 24
540 hours respectively, for all 3 entrainment periods: 90-, 130-,170-min. All organoids were

harvested at day 4 and send for RNA bulk sequencing or protein analysis. (b-g) Quantitative analysis of cell percentage per organoid compared to control (DMSO) for 90-,130- and 170-min entrainment for 72 h and representative images including percentage. Cell percentages tested for LGR5 (b, c), LYZ1 (d, e), WGA (f, g). N= minimum of 3, and n_org = minimum of 14 organoids. Normal distribution was calculated using the Shapiro Wilk test and significance was tested by independent t-test or Mann-Whitney U test depending on normal distribution. ns: 5.00e-02 < p <= 1.00e+00, *: 1.00e-02 < p <= 5.00e-02, **: 1.00e-03 < p <= 1.00e-02, ***: 1.00e-04 < p <= 1.00e-03, ****: p <= 1.00e-04. (h) Model of Hes1 oscillations determining cell proliferation and differentiation in the small intestine.

552 **Methods Summary**

553 **Extended Methods**

554 **Ethics**

555 This study complies with all relevant ethical regulations. All animal experiments were
556 approved by the Animal Experimental Committees at the Hubrecht Institute and the
557 Netherlands Cancer Institute, and the Dutch Central Authority for Scientific Procedures
558 on Animals (CCD). All animals were bred and housed under standard conditions
559 (humidity 50–60%, 22–23 °C, inverted 12/12 h light/dark cycle, water and standard
560 chow ad libitum) at the Hubrecht animal facility or at the Netherlands Cancer Institute
561 facility in Amsterdam, the Netherlands.

562

563 **Mouse model**

564 Hes1-Linker-Achilles or Hes1-Achilles (Hes1$^{tm1(Link\text{-}Achilles)Kfs}$)[4] crossed with H2B-
565 mCherry (R26-H2B-mCherry, CDB0204K)[25] or iRFPnucmem
566 (Gt(ROSA)26Sor$^{tm1(iRFPnucmem)Aau}$)[4] were used for this project. C57BL/6 mice were used
567 as controls. The H2B-mCherry mouse line was kindly provided by the Riken Center
568 for Biosystems Research, the iRFPnucmem mouse line by Alexander Aulehla (EMBL
569 Heidelberg) and the Lgr5tm2(DTR/EGFP)Fjs mouse line by Fred de Sauvage
570 (Genentech)[43]. Mice were genotyped using standard PCR procedures, for primers see
571 Supplementary Table 1.

572

573 **Paraffin sectioning of gut rolls and immunofluorescence**

574 Two males and two virgin females of 8 weeks from both the Hes1-Achilles line and
575 C57BL/6 control were used. Small intestine was isolated (from beneath the stomach
576 to the caecum) and immediately flushed with formalin 4%. The tissue was rolled and
577 stored in formalin 4% for 1 day at RT. This was followed by dehydration using a series
578 of ethanol solutions (30%, 50% and 70%). Next, the gut-rolls were soaked in Xylene,
579 embedded in paraffin and made into 5 um coupes. For staining the gut roll microscope
580 slides, the slides were soaked in Xylene, 100% ethanol, 95% ethanol, 70% ethanol,
581 50% ethanol and rinsed with running cold tab water. For antigen retrieval the slides

582 were cooked in a citrate buffer (sodium citrate (8.2mM) and citric acid (1.8mM); pH=6).
583 5% Goat Serum (cat. no. ab7481) in 0.3%-Triton PBS was used for blocking and
584 permeabilization. Primary (overnight (ON) at 4°C) and secondary antibodies (3h at
585 room temperature (RT)) were used in 0.1%BSA PBS and are listed in Supplementary
586 Table 2. After staining, gut roles were mounted with Vectashield (cat. no. H1200NB).
587 The samples were imaged using a SP8 confocal microscope (Leica Microsystems,
588 40x oil objective, numerical aperture (N.A.) = 1.3).

589

590 **Vibratome sections of small intestine**

591 One virgin female of the Hes1-Achilles background was used for this previously
592 described method[51]. In short, the small intestine was isolated (from beneath the
593 stomach to the caecum) and immediately flushed with formalin 4%. The tissue was
594 stored in formalin 4% protected from light (to maintain endogenous fluorescent signal)
595 for 1 day at RT. 1cm of tissue was embedded in 4% of low melting agarose (cat. no.
596 16520100) and sections of +/- 150 µm were made using a microtome. Microtome
597 settings included: velocity of 80mm s-1, knife amplitude of 0.70mm and vibration
598 frequency: 65Hz. Tissue slices were blocked and permeabilized with 5% Goat Serum
599 in 0.3%-Triton PBS and primary (ON at 4°C) and secondary antibodies (3h at RT) were
600 used in 0.1%BSA PBS and are listed in Supplementary Table 2. After staining, tissue-
601 slides were mounted to a microscope slide using Vectashield. The samples were
602 imaged using a SP8 confocal microscope (Leica Microsystems, 40x oil objective, N.A.
603 = 1.3).

604

605 **Organoid culture**

606 All organoids were obtained from the duodenum of male or virgin female mice older
607 than 8 weeks as described previously[52]. Organoids were embedded in BME and
608 cultured with ENR media including Advanced DMEM/F-12 (Life Technologies)
609 supplemented with; murine recombinant epidermal growth factor (50 ng/ml; Life
610 Technologies), murine recombinant Noggin (100 ng/ml; PeproTech), human
611 recombinant R-Spondin 1 (500 ng/ml; Peprotech), n-acetylcysteine (1 mM; Sigma-
612 Aldrich), N2 supplement (1×; Life Technologies) and B27 supplement (1×; Life

613 Technologies), GlutaMAX (2 mM; Life Technologies), Hepes (10 mM; Life
614 Technologies), and penicillin-streptomycin (100 U/ml; 100 µg/ml; Life Technologies).
615 For passaging, organoids were removed from BME and mechanically dissociated into
616 single-crypt domains, and then transferred to fresh BME. Passage was performed
617 every 1-2 weeks with a 1:5 split ratio. Conditions were kept stable in the incubator with
618 5% CO2 and 20% O2 at 37°C.

619

620 **2D organoid culture**

621 *Hydrogel preparation*

622 For the 2D organoid cultures, a hydrogel composed of a collagen mixture was used to
623 mimic the extracellular matrix (ECM). All materials and reagents, including Eppendorf
624 tubes, stock collagen (5 mg/mL Atelocollagen, ReproCELL, cat no. KKN-IPC-50),
625 buffers, and Matrigel, were pre-chilled on ice to prevent unwanted polymerization of
626 the precursor gel due to prolonged exposure to heat.

627 A collagen gel precursor (4 mg/mL) was prepared by neutralizing the pH of the
628 collagen stock with basic R-buffer and 10x DMEM in an 8:1:1 volume ratio. The
629 precursor was mixed by slow and gentle pipetting to avoid introducing air bubbles. The
630 phenol red in the 10x DMEM changed from yellow to light pink, indicating the shift in
631 pH of the gel precursor from acidic to basic. Due to the high viscosity of the gel
632 precursor solution, volumes were kept small, for example, 160 µL collagen stock, 20
633 µL R-buffer, and 20 µL 10x DMEM.

634 The final hydrogel mixture was prepared by combining the gel precursor with Matrigel
635 in a 4:1 volume ratio, resulting in a final concentration of 3.2 mg/mL. The mixture was
636 homogenized by slow and gentle pipetting.

637 To polymerize the hydrogel mixture, a LabTek 8-well chambered coverglass (Thermo
638 Fisher Scientific, cat. no. 155411PK) was pre-treated with plasma treatment. Prior to
639 gel transfer, the coverglass was pre-chilled on ice, preferably on a metal heating block
640 for even heat transfer, to prevent unwanted polymerization. 17.5 µL of the hydrogel
641 mixture was transferred to each chamber, ensuring even coverage of the entire bottom
642 surface. The coverglass was then immediately placed into a 37°C incubator and kept
643 for 30-min until polymerized.

644 *Seeding*

645 The 3D intestinal organoids were mechanically disaggregated by pipetting in cold
646 Advanced DMEM/F-12 (Life Technologies). For one chamber in the LabTek 8-well
647 chambered coverglass, we seeded approximately 0.7x the number of organoids
648 contained in a Matrigel drop of the 24-well plate. After disaggregation, the organoids
649 were centrifuged at 300g for 5 min at 4°C and the pellet was resuspended in ENR
650 medium. The organoids were seeded in a small volume (150 µL) in each chamber and
651 incubated at 37 °C and 5% CO2. ENR medium was refreshed every 2 days. All
652 experiments were performed 4 d after seeding.

653

654 **Microfluidic chip preparation and experiment**

655 Microfluidics experiments were performed as described previously[38,53]. In short, a
656 mold for microfluidic chips was made using a 3D printer (Atum3D) (chip design
657 available upon request). PDMS (SYLGARD #01673921/ #01673921, 1:8 ratio) was
658 poured in the mold to create the microfluidic chip. The chip and a glass slide
659 (Marienfeld, No 1.5H, high precision, 70x70 mm) were bonded using plasma treatment
660 (Diener electronic, Femto). Chip and Tubing were UV cleaned and the microfluidic chip
661 (in PBS with Pen/strep) was degassed together with the conditioned and DAPT media
662 for 4 hours. The concentration of the DAPT media depended on the pulse timing
663 (90min: 1.38µM, 130min: 2µM, 170min; 2.6µM, 2µM; for 170 min we tested two
664 different concentrations to find one that did not change oscillation amplitude or
665 absolute intensity (Fig. 4 and Extended Data Fig. 12). Organoids were passaged 3-4
666 days before performing a live-imaged microfluidic experiment for 20-24h. For the RNA
667 bulk sequencing and immunofluorescence microfluidic experiments organoids were
668 passaged 1 day before a 72h experiment, 2 days before 48h experiment and 3 days
669 before a 24h experiment. The day of the experiment, two wells of a 24-well plate were
670 harvested and washed with ice cold Advanced DMEM/F12 supplemented with
671 GlutaMAX (2 mM; Life Technologies), Hepes (10 mM; Life Technologies), and
672 penicillin-streptomycin (100 U/ml; 100 µg/ml; Life Technologies) to remove the BME.
673 Organoids are resuspended in BME to a final concentration of 50% and carefully
674 loaded into the microfluidic chip which was pre-filled with ENR culture media. After
675 loading organoids on the chip, all tubing (4x inlet tubing of 3 meters, and 2x outlet

676 tubing of 1 meter) was connected and during the experiment the organoids were
677 cultured under a flow rate of 200 µl/h, using a microfluidic pump (Harvard apparatus
678 #70-45060). After approximately 30 min culturing in culture medium, pumping program
679 to induce drug pulses was started. For the bulk RNAseq and immunofluorescence
680 microfluidic experiments, organoids were removed by aspirating the organoids out of
681 the chip with a 200ul pipet via the organoid inlets and follow-up methods were
682 performed as described.

683

684 **Time-lapse imaging**

685 *Intravital imaging*

686 Intravital imaging was performed as described in detail in Laskaris et al., 2023[54]. In
687 short: Time-lapse intravital imaging was performed on the healthy gut of Hes1-Achilles
688 reporter mice in H2B-mCherry background. Throughout the procedure, mice were
689 sedated using isoflurane inhalation anaesthesia (1.5% isoflurane/ O2 mixture). The
690 gut was surgically exposed, and the mouse was placed in a custom designed imaging
691 box with its head in a facemask constantly delivering anaesthesia. The imaging box
692 and the microscope were adjusted at 36.5°C using a climate chamber. Intravital
693 images were acquired with an inverted Leica TCS SP8 AOBS two-photon microscope
694 (Mannheim, Germany) with a chameleon Ti:Sapphire pumped Optical Parametric
695 Oscillator (Coherent Inc. Santa Clare, CA, USA). The microscopes are equipped with
696 2 non-descanned and 2 hybrid detectors: YFP and RFP were simultaneously excited
697 at 960 nm and detected with hybrid detectors. Second harmonic generation (Collagen
698 I stroma) was detected with a non-descanned detector. Images were collected every
699 10 min for a period of 3-6 hours during which the mouse was kept sedated and alive,
700 constantly hydrated with subcutaneous infusion of glucose and electrolytes (NutriFlex
701 special 70/240, Braun, 100 µl/h). All images were collected in 12 bit, 256X256 and
702 acquired with a 25X water immersion (HC FLUOTAR L N.A. 0.95 W VISIR 0.17 FWD
703 2.4 mm) objective and zoom of 1.25X.

704 *SP8 imaging of 3D organoids*

705 For Hes1-Achilles intensity analysis of crypts, organoids were passaged 3 days before
706 every live imaging experiment on an 8 chambered Lab-Tek Borosilicate microscope

707 dish with a cover glass (Thermo Fisher Scientific, cat. no. 155411PK). The organoids
708 were imaged in fresh ENR and drugs diluted in ENR were added after imaging the first
709 time point or at a later timepoint when indicated. The Leica SP8 confocal microscope
710 was used for live imaging of the organoids and were present a humid atmosphere at
711 5% CO2, 20% O2 and 37°C. The fluorescent Achilles protein was excited using a 514
712 nm laser and organoids were visualized using the 20x objective. Every 30 min images
713 were taken, using the bidirectional scanning function and a frame average of 4. To
714 visualize the full organoid, multiple images were taken from each organoid spaced by
715 z-steps of 6 µm and a pinhole of 184.5 µm (PinholeAiry of 3.26).

716 *3D organoid Light-sheet imaging*

717 Live imaging of organoids for single cell analysis was performed using a Viventis light
718 sheet microscope (Viventis microscopy #LS1 live). Imaging was performed in a humid
719 atmosphere at 5% CO2, 20% O2 and 37°C. 514, 568, 687 nm lasers were used for
720 Achilles, mCherry and iRFP, respectively and images were taken with a 25x objective.
721 A Laser beam of 2,2 µm was used and a z-stack of 100 steps of each 2 µm was taken.
722 Images were taken at 1024 x 1024 pixels every 7 min.

723 *Organoids in microfluidic chip*

724 Live imaging of organoids in the microfluidic chip was performed using a Leica SP8
725 MP or SP5 MP confocal microscope in a humid atmosphere at 5% CO2, 20% O2 and
726 37°C. Organoids were excited with a 514nm laser for Achilles through a 20x objective.
727 Every 10 min a z stack of 8µM distance was scanned at 512x512. To track given drug
728 pulses Cascade blue (cat. No. Cat#C3239) was added to the DMSO or DAPT
729 supplemented media and excited with a multi photon laser at 740nm and 3x 30µM z
730 planes were detected every 10 min at 64x64 pixels.

731 *2D organoids*

732 Four days after passaging, 2D organoids were imaged in an 8-well chambered
733 coverglass using confocal microscopy (Leica SP8) with a 25x objective. Environmental
734 conditions were set at 5% CO2, 20% O2, and 37°C with high humidity. Samples were
735 placed inside the microscope and incubated for over 2 hours before imaging to allow
736 for acclimatization. Hes1-Achilles was excited at 514 nm and H2B-mCherry at 564 nm
737 using a diode laser. Timelapse images were captured every 7 min with a resolution of

512x512 pixels at zoom 1 (pixel size: 0.36 µm), and z-steps of 0.4 µm, using a pinhole of 1 Airy unit.

Immunofluorescence of 3D-cultured organoids

Organoids in BME were fixed with 4% paraformaldehyde (freshly made at same day) for 10-45 min at RT (Supplementary Table 2), washed 3 times with PBS and blocked in PBS containing 5% Normal Goat Serum (NGS) and 0.3% Triton X-100. Samples were incubated with the primary antibodies in 1% BSA, 0.3% Triton-X100 in PBS (Supplementary Table 2) ON at 4 °C while shaking, after which the samples were washed 3 times with PBS for 10 min. The samples were incubated with Alexa conjugated secondary antibodies (1:500; Life Technologies) and DAPI (5 µg/mL, Sigma) for 3h at room temperature while shaking and subsequently washed 3 times with PBS for 10 min. The samples were imaged using a SP8 confocal microscope (Leica Microsystems, 40x oil objective, N.A. = 1.3).

Immunofluorescence of 2D-cultured organoids

2D organoids were fixed in 4% paraformaldehyde (PFA) for 20 min at room temperature (RT) and washed three times with phosphate-buffered saline (PBS). The samples were permeabilized with 0.1% Triton X-100 (Sigma-Aldrich) for 45 min at RT. After three washes with PBS, the samples were blocked with goat serum for 1 hour at RT. Primary antibodies diluted in PBS containing goat serum were added and incubated overnight at 4°C. Following three washes with PBS, secondary antibodies in PBS containing 10% goat serum were added and incubated for 2 hours at RT. After three additional washes in PBS, wheat germ agglutinin (WGA) diluted to 1:500 in PBS was added for 1 hour at RT. Finally, the samples were washed three times with PBS (5 min each) and imaged.

Image and data processing

Gut-rolls were analysed using Fiji and graphs were plotted with Prism.

767 Microfluidic time series were analysed using a Fiji Macro, based on manual tracking
768 of a ROI and plotted in Python. Quantification of crypt oscillatory dynamics was
769 performed by using PyBOAT (settings: min_period=50, max_period=400, TC=200).

770 Kymographs were created as follows: First, a maximum intensity projection was
771 performed on all z-planes. The time series data were then smoothed using a Gaussian
772 filter (2 scaled units). Kymographs were constructed along a user-defined line
773 extending from the crypt to the villus using the Fiji[55] plugin KymoResliceWide (intensity
774 averaged over the width of a 50 px wide line). These kymographs were further
775 smoothed using a Gaussian filter with 2 scaled units.

776 Intravital imaging images were manually corrected in XY using a Fiji plug-in
777 Bigdataprocessor2. Z correction and single-cell tracking was manually performed in
778 Mastodon a Fiji plug-in. Single-cell tracks were plotted in phyton.

779 3D organoid light-sheet images were cropped and registered using LStree[56]. Single
780 cells were manually tracked using Mastodon. Hes1-Achilles intensity was normalized
781 to the global mean of Hes1-Achilles per experiment. Graphs were plotted with Python
782 and quantification of oscillation dynamics was performed using pyBOAT (settings:
783 min_period=50, max_period=400, TC=200) and Python.

784 Image Analysis of stainings and markers after microfluidics and average DAPT
785 included (Fig. 5 & Extended Data Fig. 16, 17):

786 1. Organoid segmentation

787 Image analysis was performed using Python 3 and Scikit-image [scikit-image 0.24.0
788 (2024-06-18)]. Organoids were segmented from each acquired z-stack based on the
789 DAPI channel. For each plane, a mask was generated by applying a Gaussian blur
790 and binarization with a threshold that was set at 2 times the mean DAPI intensity of
791 the plane. Following binarization, masks with fewer than 2000 pixels were excluded
792 from the analysis. All pixels outside the mask were set to zero. Maximum intensity
793 projections (MIPs) were generated from all planes and used for further analysis. For
794 each segmented organoid, the area and the mean intensity of markers was calculated.

795 2. Superpixel analysis on organoid masks

Superpixel analysis was conducted following the protocol established by Suppinger et al. (2023)[57]. The DAPI mask in each image was considered as the total superpixel value, with each superpixel approximating the size of a single cell, approximately 250 pixels. Superpixels served as proxies for individual cells to quantify the presence of LGR5, WGA, SOX9, LYZ1, and SCA-1 expressing cells. The mean intensity of the markers in superpixels in control organoids (DMSO) was used as a threshold to identify positive superpixels in the test condition (DAPT-treated). The percentage of positive superpixels was then calculated relative to the total number of superpixels per cell type marker. Additionally, enterocyte percentages were inferred by subtracting LGR5+ and WGA+ [and SOX9+] superpixels from the total number. To ensure that our analysis was focused on homeostasis, all organoids smaller than 100000 pixels were excluded from the analysis. This size exclusion threshold was based on manual selection.

2D image analysis

Segmentation and tracking

Nuclear annotation was performed using Cellpose with the “nuclei” model as a starting point. A total of 306 images was annotated in each xy, xz, and yz planes. The annotations generated by Cellpose served as ground truths to train Stardist, ensuring star-convex shapes for nuclei.

Cell tracking was conducted using the Laptrack algorithm in Python. Tracks were manually verifying in high-division zones near the crypt centres, addressing segmentation errors that often occurred during cell division. The Laptrack-generated tracks were converted to GraphML files and manually verified using Mastodon, a plugin for Fiji.

Cell Type Classification

To classify cell types by backtracking from endpoint stainings, the last frame of live imaging was manually aligned to endpoint IF stainings. Cells in this frame were manually annotated per cell type in Napari software in Python. Custom Python code allowed cell type back-tracking with the following rules:

1. Stem cells are OLMF4+ and the mother cells of stem cells are stem cells, assuming the directionality of differentiation.

2. Secretory cells are WGA+
3. Paneth cells are WGA+, adjacent to stem cells and do not divide [35] during the 24-hour imaging period

Using these definitions, we calculated the distance from the crypt centre as the number of cells away from Paneth cells (Fig. 2)

4. IMPCs are mothers of secretory cells or mothers of Hes1-Achilles low cells within the crypt (<4 cells aways from Paneth cells) which lacked the WGA marker.

We assumed that these WGA-negative cells are in fact IMPCs that have committed to their fate but have not yet produced mucin detectable by WGA. Or they belong to a rare secretory lineage such as enteroendocrine cells. However, given the statistical improbability of their being rare cell types, we classified them as IMPCs.

5. Enterocytes are Hes1-Achilles low cells (track intensity median below threshold = 0.075), 2) WGA negative and 3) far away (>3 cells) from Paneth cells.

Based on our staining for enterocytes in 2D cultures (Extended Data Fig. 6), we know that enterocytes make up of most of the non-secretory, Hes1-Achilles low cells residing on the outside of the crypt zone.

6. TA cells are Hes1-Achilles positive cells residing between stem cells and enterocytes
    a. Early TA are Hes1-Achilles high and up to 3 cells away from Paneth cells
    b. Late TA are Hes1-Achilles high and 4 cells or more away from Paneth cells.

Hes1-Achilles Intensity Track Analysis

All analysis was performed using custom-written Python code. To standardize Hes1-Achilles intensities across datasets, intensities were normalized to the minimum and maximum values of each dataset. Tracks were smoothed with a moving mean across three time points to remove non-biological noise.

Fourier transform was performed for each track, and then the fundamental and the first harmonic contributions were removed for each track to isolate genuine oscillatory

signals. Mean power spectrum was generated across all tracks. Wavelet analysis was implemented using PyBOAT, with a minimum and maximum period (Tc) set to 200. The period of best fit was calculated using ridge detection within the PyBOAT algorithm. Neighbourhood analysis was adapted from methods available on Robert Haase's GitHub repository. Calculation of the Kuramoto order parameter was adapted from the Arnold-Tongue paper.

To detect transition events, we selected a subset of tracks that had low Hes1-Achilles intensities (<0.075 AU) in the last 20 frames (140 min). We then applied a rolling median of 10 timepoints (70 min) to Hes1-Achilles reporter intensities in each track to reduce noise. We defined the time when this median first becomes >0.1 AU as the transition point.

Statistical Analysis

For all experiments at least three independent experiments were performed. To visualize data, Tukey style boxplots were used (bar=median, box=25th and 75th percentile, whiskers=1.5*IQR). Data displayed as violin plots present data from max to min with bar=median. For statistical comparisons between groups, normal distribution was calculated by Shapiro-Wilk testing. Significance was tested by independent t-test or Mann-Whitney U test depending on normal distribution. To correct for multiple groups Bonferroni calculation was used.

RNAseq quantification and Statistical Analysis

Organoids (20-50 organoids per sample) were harvested from the microfluidic chip. Total RNA was isolated using TRIzol Reagent (Invitrogen, #15596018). In brief, samples were barcoded with CEL-seq2 primers during a reverse transcription and pooled after second strand synthesis. The resulting cDNA was amplified with an overnight *in vitro* transcription reaction. From this amplified RNA, sequencing libraries were prepared with Illumina Truseq small RNA-primers. The DNA library was paired-end sequenced on an Illumina NextSeq™ 500, high output, with a 1x75 bp Illumina kit (R1: 26 cycles, index read: 6 cycles, R2: 60 cycles). Reads that mapped equally well

887 to multiple locations were discarded. Mapping and generation of count tables was
888 done using the STARSolo 2.7.10b aligner.

889

890 **Bulk RNAseq mapping and analysis**

891 Resulting bulk RNAseq data were mapped to the mouse genome (mm38) using STAR
892 (version 2.7.8a). umi_tools (version 1.1.1) was used to collapse PCR-amplified reads
893 into distinct transcripts. Samples with less than 500,000 transcripts were determined
894 as low quality and discarded from further analysis, resulting in median depth of
895 960,086 transcripts per sample. To generate heatmaps (Figure 5b, Extended Data
896 Figures 15a-b), data was size normalized, and each sample was compared to the
897 time-matched DMSO controls.

898

899 **Reanalysis of single-cell RNAseq data**

900 Single-cell RNAseq data from Bues et al. (2022)[40] were downloaded and re-clustered
901 with the Metacell package, as described before[58]. Cells with less than 400 UMI or more
902 than 20,000 UMI were treated as low quality or doublets and discarded from analysis,
903 resulting in 2,285 total cells retained for clustering analysis.

904 We selected genes as features for the metacell algorithm using the parameters
905 Tvm=0.06, total umi > 5, and more than 4 UMI in at least 3 cells. We filtered the list of
906 gene features from genes associated with cell cycle or immediate stress response.
907 For this, we first identified all genes with a correlation coefficient of at least 0.12 for
908 one of the anchor genes *Top2a*, *Ube2c*, *Mki67*, *Pcna*, *Mcm4*, *Egr1*, *Fos*, and *Jun*. We
909 then hierarchically clustered the correlation matrix between these genes and selected
910 the gene clusters containing the above anchor genes. We thus retained 153 genes as
911 features. We used Metacell to build a kNN graph, perform boot-strapped co-clustering
912 (500 iterations; resampling 70% of the cells in each iteration), and derive a cover of
913 the co-clustering kNN graph (K=20). We manually split meta-cells that mixed goblet
914 and Paneth cell signatures by clustering these cells based on gene modules correlated
915 with *Muc2* (goblet cells) and *Lyz1* (Paneth cells).

916 scRNAseq Data from Haber et al. (2017)[12] were downloaded and harmonized with the
917 Bues et al. dataset as follows: For each single cell in Haber et al. (representing
918 wildtype organoids grown in ENR only), we computed the K (K = 10) nearest neighbors
919 from Bues et al. based on Pearson correlation. Then meta-cell assignment for each
920 cell in Haber et al. was determined by majority voting.

921

922 **LDA-based bulk RNAseq deconvolution**

923 We applied a Latent Dirichlet Allocation (LDA)-based approach to predict cell type
924 distribution of samples in the bulk RNAseq dataset[59]. Whereas in conventional LDA
925 analysis, both the distribution of topics as well as the probabilities of observing words
926 within topics are determined concurrently, here, we used predetermined topics
927 extracted from analysis of a reference scRNAseq dataset. Thus, each metacell in the
928 reanalysis of Bues et al. represents a topic, whose words (i.e., genes) distributions is
929 calculated as a multinomial probability distribution. We use the LDA algorithm
930 (topicmodels version 0.2-9) with a predetermined beta matrix, in order to optimize the
931 distribution of topics per text (i.e., metacells per bulk sample). We selected a subset
932 of the genes and used them as features for the LDA as follows: We selected for each
933 metacell the top 30 most enriched genes, given they have at least 0.7 enrichment
934 score ($\log_2$ fold-change over the median expression), and at least 100 UMI across all
935 single cells and at least 1,000 transcripts in the bulk dataset. This resulted in a set of
936 342 genes used as features. To increase reproducibility, we reran the LDA 100 times,
937 each time with a slightly altered beta matrix. The beta matrix (representing the words
938 per topic multinomial distributions) in each iteration was calculated over a sample of
939 the single cells (representing 70% of cells per meta-cell). We then extracted the
940 median value per meta-cell.

941 We sought to test the performance of this approach across two unrelated datasets.
942 For this purpose, we tested our ability to deconvolve pseudo-bulk aggregates
943 generated from Haber et al. (generated with the 10x genomics platform), using Bues
944 et al. (generated by the DisCo technology) as a single-cell RNAseq reference. We first
945 harmonized the two datasets as described above. Then, we generated 100 pseudo-
946 bulk aggregates of 200 cells from Haber et al., mixing cell types at varying proportions.
947 We used our LDA approach to infer cell type proportions for each aggregate and

compared them to the ground truth. We report high agreement between inferred and ground-truth levels of Enterocytes (R^2 0.85), Enteroendocrine cells (0.78), Goblet cells (0.72) and Paneth cells (0.88), whereas stem cells and TA cell levels could not be faithfully inferred (R^2=0.17 and 0.15, respectively), probably due to them lacking a clear transcriptional signature.

Data and Code availability

All data and custom code used in this study are available upon request to k.sonnen@hubrecht.eu.

Acknowledgements

We thank all members of the Sonnen, Bothma and Garaycoechea labs for discussions and Juan Garaycoechea and Takashi Hiiragi for feedback on the manuscript. We thank Ben Simons, François Schweisguth, Johan van Es and Hans Clevers for insightful discussions, Joep Beumer for advice when setting up organoid culture in the lab, Jean-Yves Tinevez for developing a beta-version of Mastodon, Mike Nikolaev, Nikolce Gjorevski and Matthias Lütolf for support with setting up the 2D organoid culture and Yasmine el Azhar for providing mice. We thank Wouter Thomas, Jeroen Korving, Benaissa el Haddouti, Stieneke van den Brink and Maria Azkanaz for technical help. We are grateful to Jos Malda for sharing microfabrication equipment and Andrea Boni (Viventis) for advice. This work was supported by the Hubrecht imaging and animal facilities and the NKI animal facility. The H2B-mCherry was kindly provided by the Riken Centre for Biosystems Dynamics Research, the Lgr5tm2(DTR/EGFP)Fjs mouse line by Fred de Sauvage, Genentech, and the iRFPnucmem reporter by Alexander Aulehla. This work was supported by the Hubrecht Institute and received funding from the European Research Council under an ERC starting grant agreement no. 850554 and KWF grants 13661 and 15261 to K.F.S.

Author contributions

Conceptualization: S.W., H.E. and K.F.S., Methodology: S.W., H.E., K.A, E.L., M.H., W.B., Software: H.E., J.L. and A.G. Formal Analysis: S.W., H.E., J.L., A.G. and K.F.S., Investigation: S.W., H.E., Writing: S.W., H.E. and K.F.S., Review and Editing: S.W., H.E., J.L., A.G., J.R., A.O. and K.F.S., Supervision: J.R., A.O. and K.F.S., Project administration and Funding acquisition: K.F.S.

References

1 Pellegrinet, L. *et al.* Dll1- and dll4-mediated notch signaling are required for homeostasis of intestinal stem cells. *Gastroenterology* **140**, 1230-1240.e1231-1237 (2011). https://doi.org/10.1053/j.gastro.2011.01.005

2 Fre, S. *et al.* Notch signals control the fate of immature progenitor cells in the intestine. *Nature* **435**, 964-968 (2005). https://doi.org/10.1038/nature03589

3 Gehart, H. & Clevers, H. Tales from the crypt: new insights into intestinal stem cells. *Nat Rev Gastroenterol Hepatol* **16**, 19-34 (2019). https://doi.org/10.1038/s41575-018-0081-y

4 Azhar, Y. e. *et al.* Unravelling differential Hes1 dynamics during axis elongation of mouse embryos through single-cell tracking. *bioRxiv*, 2024.2003.2030.586691 (2024). https://doi.org/10.1101/2024.03.30.586691

5 Darwich, A. S., Aslam, U., Ashcroft, D. M. & Rostami-Hodjegan, A. Meta-Analysis of the Turnover of Intestinal Epithelia in Preclinical Animal Species and Humans. *Drug Metabolism and Disposition* **42**, 2016-2022 (2014). https://doi.org/10.1124/dmd.114.058404

6 Stevens, C. E. C. Rate of renewal of the cells of the intestinal epithelium in the rat. *The Anatomical record* **97** (1947).

7 Beumer, J. & Clevers, H. Cell fate specification and differentiation in the adult mammalian intestine. *Nature Reviews Molecular Cell Biology* **22**, 39-53 (2021). https://doi.org/10.1038/s41580-020-0278-0

8 Spit, M., Koo, B. K. & Maurice, M. M. Tales from the crypt: intestinal niche signals in tissue renewal, plasticity and cancer. *Open Biol* **8** (2018). https://doi.org/10.1098/rsob.180120

9 van Es, J. H. *et al.* Dll1+ secretory progenitor cells revert to stem cells upon crypt damage. *Nature Cell Biology* **14**, 1099-1104 (2012). https://doi.org/10.1038/ncb2581

10 Wang, Y. *et al.* Single-cell transcriptome analysis reveals differential nutrient absorption functions in human intestine. *J Exp Med* **217** (2020). https://doi.org/10.1084/jem.20191130

11 Garabedian, E. M., Roberts, L. J., McNevin, M. S. & Gordon, J. I. Examining the role of Paneth cells in the small intestine by lineage ablation in transgenic mice. *J Biol Chem* **272**, 23729-23740 (1997). https://doi.org/10.1074/jbc.272.38.23729

12 Haber, A. L. *et al.* A single-cell survey of the small intestinal epithelium. *Nature* **551**, 333-339 (2017). https://doi.org/10.1038/nature24489

13 Sancho, R., Cremona, C. A. & Behrens, A. Stem cell and progenitor fate in the mammalian intestine: Notch and lateral inhibition in homeostasis and disease. *EMBO reports* **16**, 571-581 (2015). https://doi.org/https://doi.org/10.15252/embr.201540188

14 Jensen, J. *et al.* Control of endodermal endocrine development by Hes-1. *Nat Genet* **24**, 36-44 (2000). https://doi.org/10.1038/71657

15 Suzuki, K. *et al.* Hes1-deficient mice show precocious differentiation of Paneth cells in the small intestine. *Biochem Biophys Res Commun* **328**, 348-352 (2005). https://doi.org/10.1016/j.bbrc.2004.12.174

16 Sonnen, K. F. & Janda, C. Y. Signalling dynamics in embryonic development. *Biochem J* **478**, 4045-4070 (2021). https://doi.org/10.1042/BCJ20210043

17 Sonnen, K. F. & Aulehla, A. Dynamic signal encoding--from cells to organisms. *Semin Cell Dev Biol* **34**, 91-98 (2014). https://doi.org/10.1016/j.semcdb.2014.06.019

18 Hirata, H. *et al.* Oscillatory expression of the bHLH factor Hes1 regulated by a negative feedback loop. *Science* **298**, 840-843 (2002). https://doi.org/10.1126/science.1074560

19 Seymour, P. A. *et al.* Jag1 Modulates an Oscillatory Dll1-Notch-Hes1 Signaling Module to Coordinate Growth and Fate of Pancreatic Progenitors. *Dev Cell* **52**, 731-747.e738 (2020). https://doi.org/10.1016/j.devcel.2020.01.015

20 Shimojo, H., Ohtsuka, T. & Kageyama, R. Oscillations in notch signaling regulate maintenance of neural progenitors. *Neuron* **58**, 52-64 (2008). https://doi.org/10.1016/j.neuron.2008.02.014

21 Lahmann, I. *et al.* Oscillations of MyoD and Hes1 proteins regulate the maintenance of activated muscle stem cells. *Genes & development* **33**, 524-535 (2019). https://doi.org/10.1101/gad.322818.118

22 Kay, S. K. *et al.* The role of the Hes1 crosstalk hub in Notch-Wnt interactions of the intestinal crypt. *PLoS Comput Biol* **13**, e1005400 (2017). https://doi.org/10.1371/journal.pcbi.1005400

23 Singh, P. N. P. *et al.* Transcription factor dynamics, oscillation, and functions in human enteroendocrine cell differentiation. *Cell Stem Cell* **31**, 1038-1057 e1011 (2024). https://doi.org/10.1016/j.stem.2024.04.015

24 Fre, S. *et al.* Notch Lineages and Activity in Intestinal Stem Cells Determined by a New Set of Knock-In Mice. *PLOS ONE* **6**, e25785 (2011). https://doi.org/10.1371/journal.pone.0025785

25 Abe, T. *et al.* Establishment of conditional reporter mouse lines at ROSA26 locus for live cell imaging. *Genesis* **49**, 579-590 (2011). https://doi.org/10.1002/dvg.20753

26 Stamataki, D. *et al.* Delta1 Expression, Cell Cycle Exit, and Commitment to a Specific Secretory Fate Coincide within a Few Hours in the Mouse Intestinal Stem Cell System. *PLOS ONE* **6**, e24484 (2011). https://doi.org/10.1371/journal.pone.0024484

27 Daub, H. *et al.* Kinase-selective enrichment enables quantitative phosphoproteomics of the kinome across the cell cycle. *Mol Cell* **31**, 438-448 (2008). https://doi.org/10.1016/j.molcel.2008.07.007

28 Masamizu, Y. *et al.* Real-time imaging of the somite segmentation clock: revelation of unstable oscillators in the individual presomitic mesoderm cells. *Proc Natl Acad Sci U S A* **103**, 1313-1318 (2006). https://doi.org/10.1073/pnas.0508658103

29 Schmal, C., Monke, G. & Granada, A. E. Analysis of Complex Circadian Time Series Data Using Wavelets. *Methods Mol Biol* **2482**, 35-54 (2022). https://doi.org/10.1007/978-1-0716-2249-0_3

30 Perez-Gonzalez, C. *et al.* Mechanical compartmentalization of the intestinal organoid enables crypt folding and collective cell migration. *Nat Cell Biol* **23**, 745-757 (2021). https://doi.org/10.1038/s41556-021-00699-6

31 Sanman, L. E. *et al.* Generation and Quantitative Imaging of Enteroid Monolayers. *Methods Mol Biol* **2171**, 99-113 (2020). https://doi.org/10.1007/978-1-0716-0747-3_6

32 Gjorevski, N. *et al.* Tissue geometry drives deterministic organoid patterning. *Science* **375**, eaaw9021 (2022). https://doi.org/10.1126/science.aaw9021

33 Blache, P. *et al.* SOX9 is an intestine crypt transcription factor, is regulated by the Wnt pathway, and represses the CDX2 and MUC2 genes. *J Cell Biol* **166**, 37-47 (2004). https://doi.org/10.1083/jcb.200311021

34 Isomura, A. & Kageyama, R. Ultradian oscillations and pulses: coordinating cellular responses and cell fate decisions. *Development* **141**, 3627-3636 (2014). https://doi.org/10.1242/dev.104497

35 Zheng, X. *et al.* Organoid cell fate dynamics in space and time. *Sci Adv* **9**, eadd6480 (2023). https://doi.org/10.1126/sciadv.add6480

36 Tian, H. *et al.* A reserve stem cell population in small intestine renders Lgr5-positive cells dispensable. *Nature* **478**, 255-259 (2011). https://doi.org/10.1038/nature10408

37 Pikovsky, A., Rosenblum, M. & Kurths, J. *Synchronization : a universal concept in nonlinear sciences*. (Cambridge University Press, 2001).

38 Sanchez, P. G. L. *et al.* Arnold tongue entrainment reveals dynamical principles of the embryonic segmentation clock. *Elife* **11** (2022). https://doi.org/10.7554/eLife.79575

39 Sonnen, K. F. *et al.* Modulation of Phase Shift between Wnt and Notch Signaling Oscillations Controls Mesoderm Segmentation. *Cell* **172**, 1079-1090.e1012 (2018). https://doi.org/10.1016/j.cell.2018.01.026

40 Pikovsky, A., Rosenblum, M., Kurths, J. & Synchronization, A. A universal concept in nonlinear sciences. *Self* **2**, 3 (2001).

41 Bues, J. *et al.* Deterministic scRNA-seq captures variation in intestinal crypt and organoid composition. *Nature Methods* **19**, 323-330 (2022). https://doi.org/10.1038/s41592-021-01391-1

42 Mustata, R. C. *et al.* Identification of Lgr5-independent spheroid-generating progenitors of the mouse fetal intestinal epithelium. *Cell Rep* **5**, 421-432 (2013). https://doi.org/10.1016/j.celrep.2013.09.005

43 Ayyaz, A. *et al.* Single-cell transcriptomes of the regenerating intestine reveal a revival stem cell. *Nature* **569**, 121-125 (2019). https://doi.org/10.1038/s41586-019-1154-y

44 Marinopoulou, E. *et al.* HES1 protein oscillations are necessary for neural stem cells to exit from quiescence. *iScience* **24**, 103198 (2021). https://doi.org/10.1016/j.isci.2021.103198

45 Sabherwal, N. *et al.* Differential phase register of Hes1 oscillations with mitoses underlies cell-cycle heterogeneity in ER(+) breast cancer cells. *Proc Natl Acad Sci U S A* **118** (2021). https://doi.org/10.1073/pnas.2113527118

46 Ochi, S., Imaizumi, Y., Shimojo, H., Miyachi, H. & Kageyama, R. Oscillatory expression of Hes1 regulates cell proliferation and neuronal differentiation in the embryonic brain. *Development* **147** (2020). https://doi.org/10.1242/dev.182204

47 Maeda, Y., Isomura, A., Masaki, T. & Kageyama, R. Differential cell-cycle control by oscillatory versus sustained Hes1 expression via p21. *Cell Rep* **42**, 112520 (2023). https://doi.org/10.1016/j.celrep.2023.112520

48 Clevers, H., Loh, K. M. & Nusse, R. Stem cell signaling. An integral program for tissue renewal and regeneration: Wnt signaling and stem cell control. *Science* **346**, 1248012 (2014). https://doi.org/10.1126/science.1248012

49 Ponsioen, B. *et al.* Quantifying single-cell ERK dynamics in colorectal cancer organoids reveals EGFR as an amplifier of oncogenic MAPK pathway signalling. *Nat Cell Biol* **23**, 377-390 (2021). https://doi.org/10.1038/s41556-021-00654-5

50 Muta, Y. *et al.* Composite regulation of ERK activity dynamics underlying tumour-specific traits in the intestine. *Nat Commun* **9**, 2174 (2018). https://doi.org/10.1038/s41467-018-04527-8

51 Snippert, H. J., Schepers, A. G., Delconte, G., Siersema, P. D. & Clevers, H. Slide preparation for single-cell–resolution imaging of fluorescent proteins in their three-dimensional near-native environment. *Nat Protoc* **6**, 1221-1228 (2011). https://doi.org/10.1038/nprot.2011.365

52 Sato, T. *et al.* Single Lgr5 stem cells build crypt-villus structures in vitro without a mesenchymal niche. *Nature* **459**, 262-265 (2009). https://doi.org/10.1038/nature07935

53 van Oostrom, M. J., Meijer, W. H. M. & Sonnen, K. F. A Microfluidics Approach for the Functional Investigation of Signaling Oscillations Governing Somitogenesis. *J Vis Exp* **169**, 1-17 (2021). https://doi.org/10.3791/62318

54 Rheenen, J. v. *et al.* Laser Ablation and Intravital Microscopy to Study Intestinal Remodeling. *JoVE*, e64756 (2023). https://doi.org/doi:10.3791/64756

55 Schindelin, J. *et al.* Fiji: an open-source platform for biological-image analysis. *Nat Methods* **9**, 676-682 (2012). https://doi.org/10.1038/nmeth.2019

56 de Medeiros, G. *et al.* Multiscale light-sheet organoid imaging framework. *Nat Commun* **13**, 4864 (2022). https://doi.org/10.1038/s41467-022-32465-z

57 van der Walt, S. *et al.* scikit-image: image processing in Python. *PeerJ* **2**, e453 (2014). https://doi.org/10.7717/peerj.453

58 Medaglia, C. *et al.* Spatial reconstruction of immune niches by combining photoactivatable reporters and scRNA-seq. *Science* **358**, 1622-1626 (2017). https://doi.org/10.1126/science.aao4277

59 Yang, Q. *et al.* An interpretable single-cell RNA sequencing data clustering method based on latent Dirichlet allocation. *Brief Bioinform* **24** (2023). https://doi.org/10.1093/bib/bbad199

60 metacell: Meta cell analysis for single cell RNA-seq data (2021).

1137

Supplementary Information

Supplemental information contains 17 Extended Data Figures, 2 supplemental tables and 10 supplemental movies.

Extended Data Fig. Legends

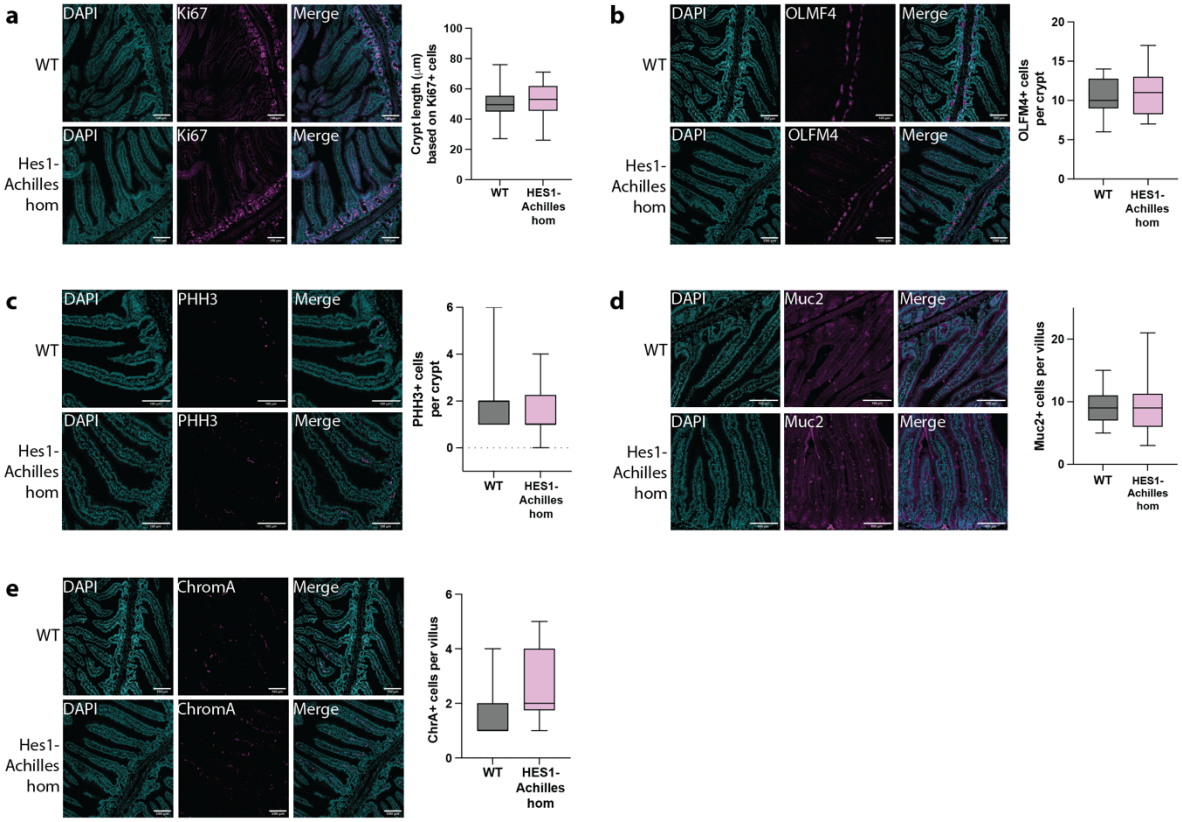

Extended Data Fig. 1. Characterization of the small intestine in Hes1-Achilles reporter mice. Representative images of WT and Hes1-Achilles gut-rolls immuno-stained for a proliferative marker Ki67 (a) or TA cell marker OLMF4 (b) or mitotic marker PHH3 (c) or goblet cell marker Muc2 (d), or enteroendocrine cell marker ChrA (e) and counterstained with DAPI. The length (a), amount per crypt (b, c) or amount per villus (d, e) of cell marker signal was quantified in WT and Hes1-Achilles gut rolls. 2 male and 2 female mice were used for both conditions and 3 crypts or villi were used to sample the cells or crypt size. No significant differences were detected. Normal distribution was calculated by Shapiro Wilk test and significance was tested by independent t-test or Mann-Whitney U test depending on normal distribution. ns: 5.00e-02 < p <= 1.00e+00, *: 1.00e-02 < p <= 5.00e-02, **: 1.00e-03 < p <= 1.00e-02, ***: 1.00e-04 < p <= 1.00e-03, ****: p <= 1.00e-04.

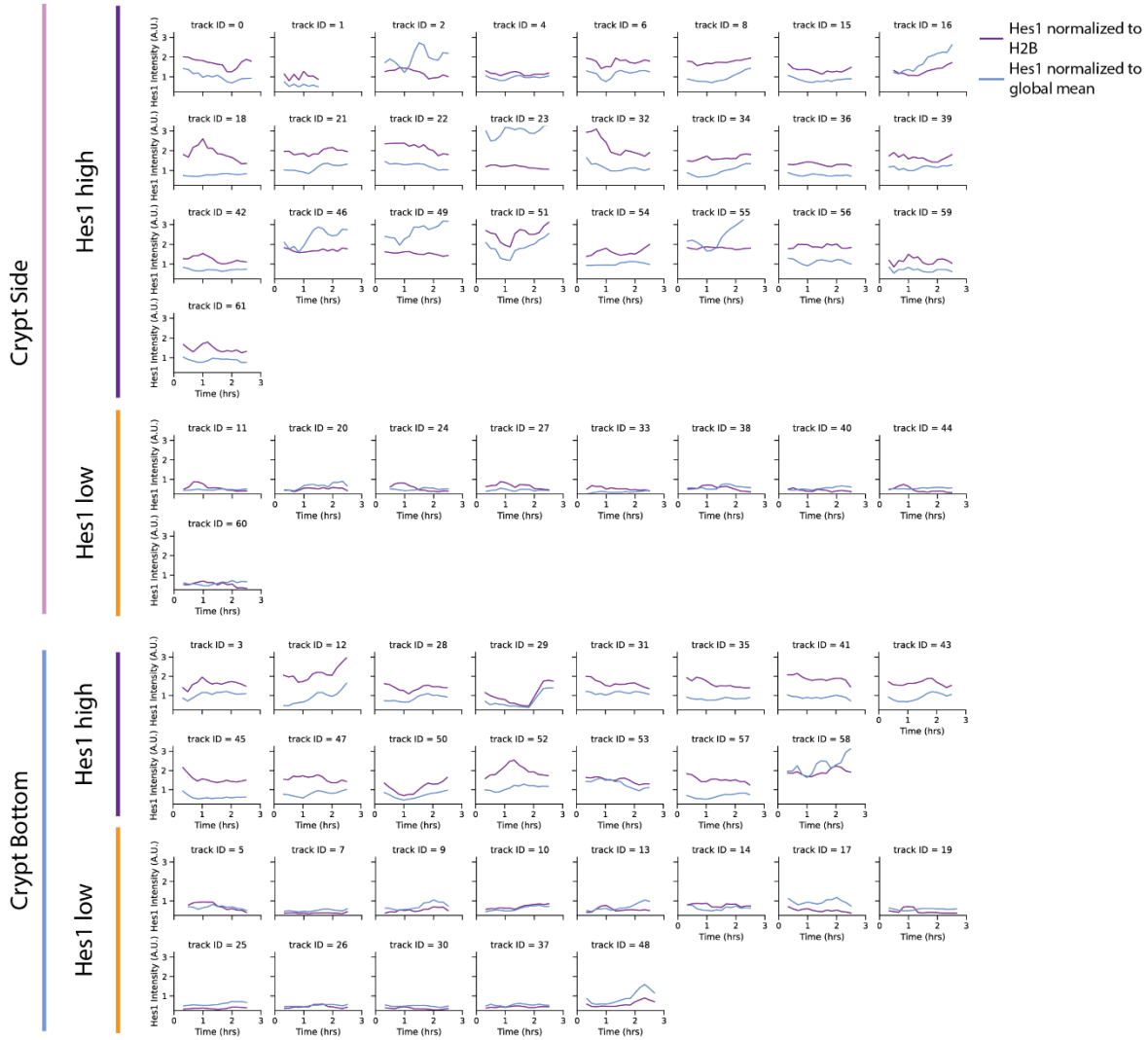

Extended Data Fig. 2. Single-cell tracks measured in small intestinal crypts *in vivo*. Hes1-Achilles mean-normalised (blue) and Hes1-Achilles H2B normalized (purple) timeseries data of single cells obtained by intravital imaging of the small intestine (N=1, n_crypt=4). Tracks have been manually subdivided into crypt bottom and side (total n=62 tracks), and clustered on Hes1-Achilles low (Hes1-Achilles H2B normalized <0.8) and Hes1-Achilles high (Hes1-Achilles H2B normalized >0.8).

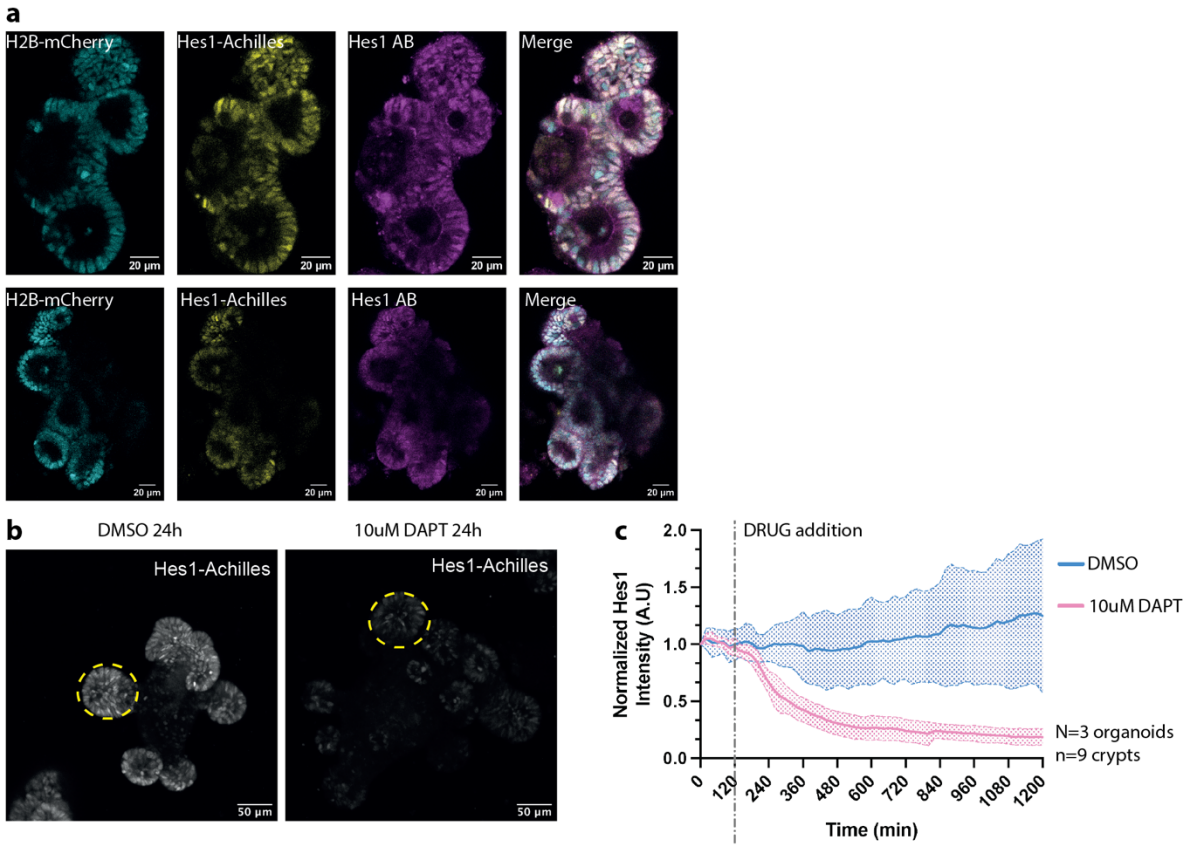

Extended Data Fig. 3. Hes1 expression is NOTCH dependent in intestinal organoids. (a) Representative images of Hes1-Achilles small intestinal organoids, with nuclear marker H2B-mCherry, immuno-stained for Hes1. (b) Representative images of small intestinal organoids treated with DMSO (control) or the gamma-secretase inhibitor DAPT after 24 hours. (c) Hes1-Achilles intensity (normalised to first 120 timepoints of DMSO) was measured over time. Dotted line represents the SD and solid line represents the mean of 9 crypts tracked in 3 organoids. Grey line represents treatment start time of 120 min.

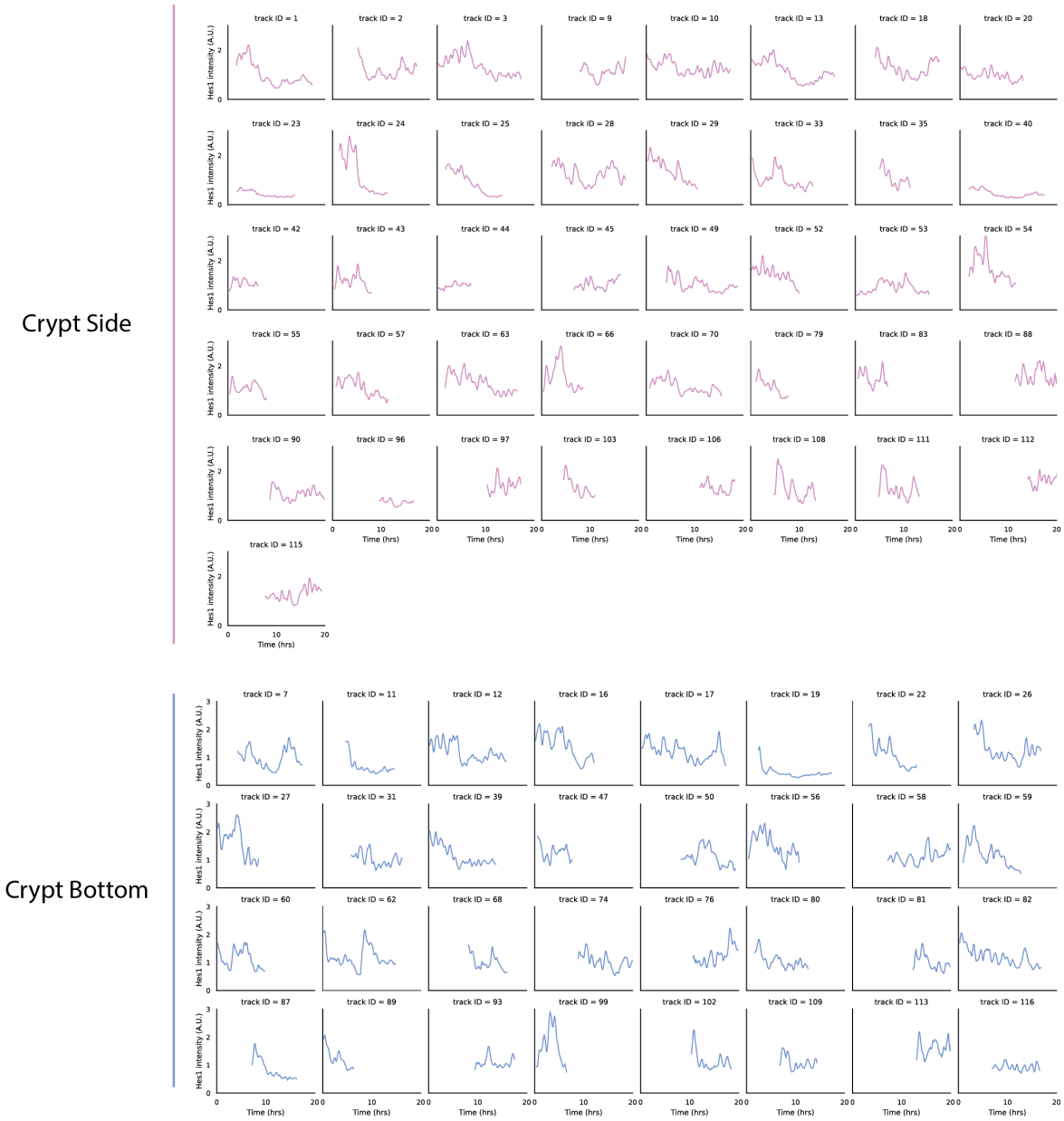

Extended Data Fig. 4. Tracks of single cells in crypts of Hes1-Achilles intestinal organoids. Mean-normalised and detrended timeseries data of single cells analysed in Fig. 1i, j (N=3). Single-cell tracks are manually subdivided into crypt bottom (n=32) and side cells (n=41).

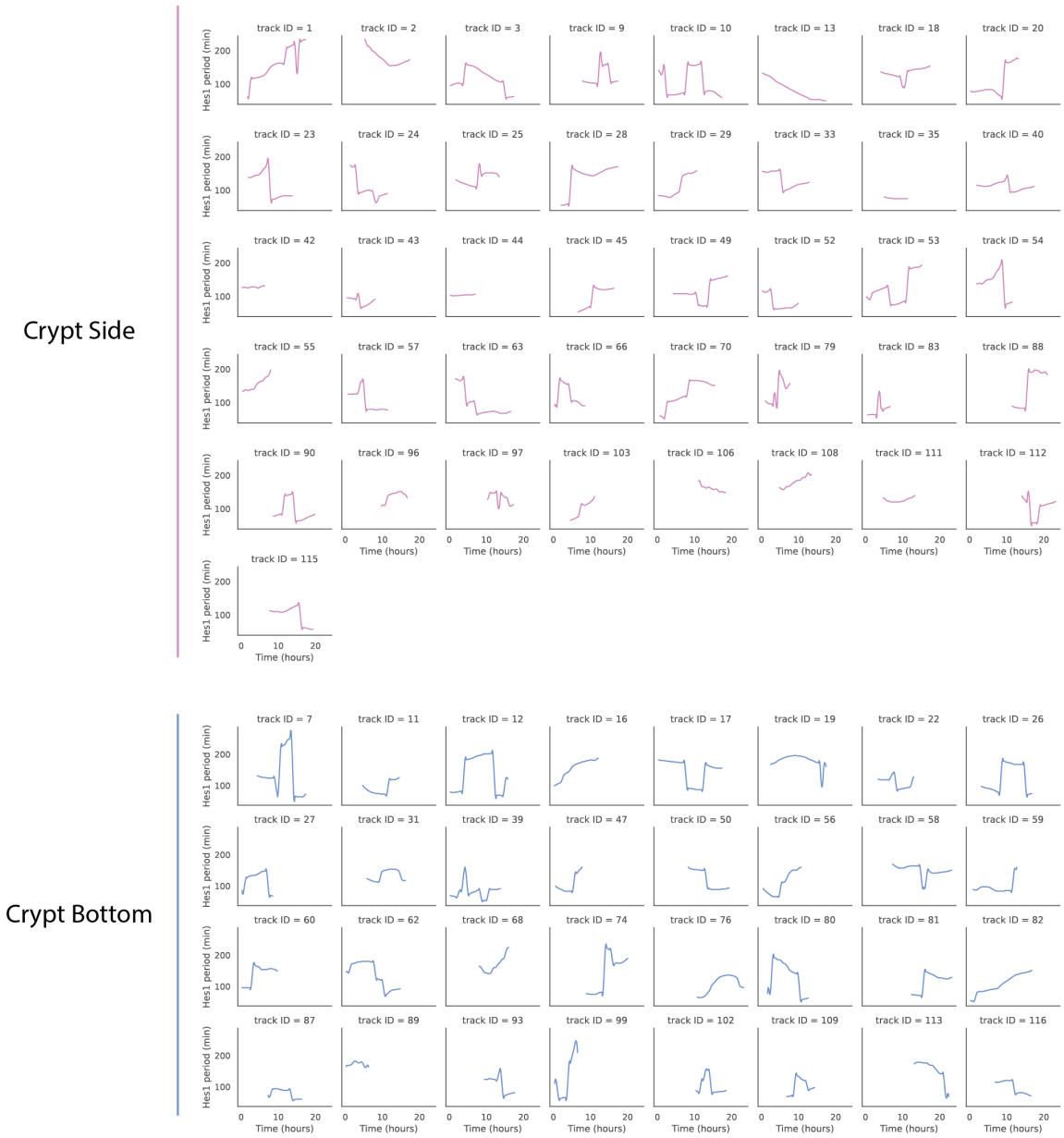

Extended Data Fig. 5. Instantaneous period of single cells in crypts of Hes1-Achilles intestinal organoids. Period quantified by wavelet transform over time which is plotted in Fig. 1k (N=3). Single cell period tracks are subdivided into crypt bottom (n=32) and side cells (n=41).

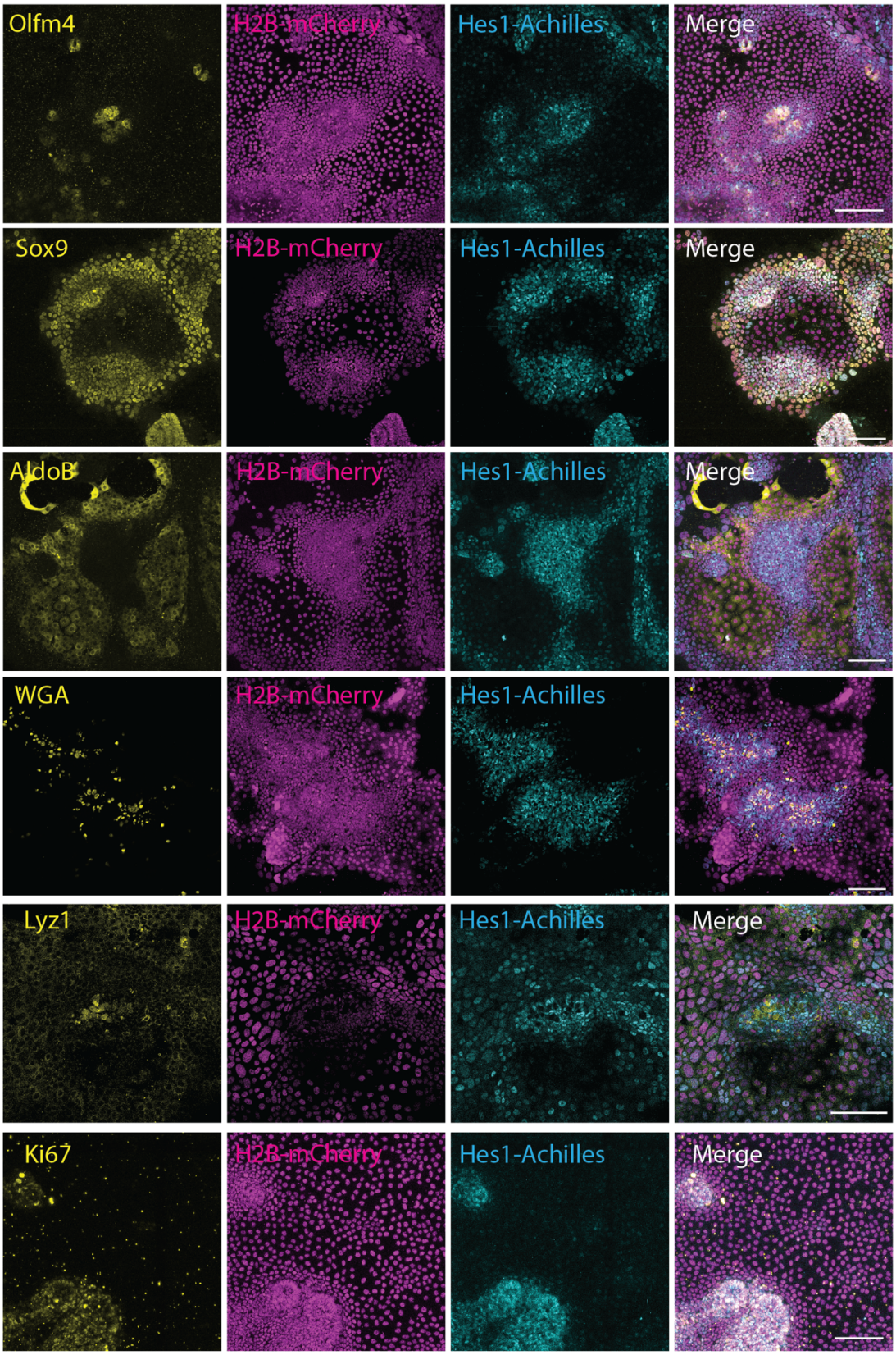

Extended Data Fig. 6. Immunofluorescent staining of cell-type markers. Intestinal organoids expressing Hes1-Achilles and H2B-mCherry were cultured in 2D, followed

1189 by IF stainings for the indicated markers as well as WGA staining. Representative
1190 images are shown. Scale bar 50 µm.

1191

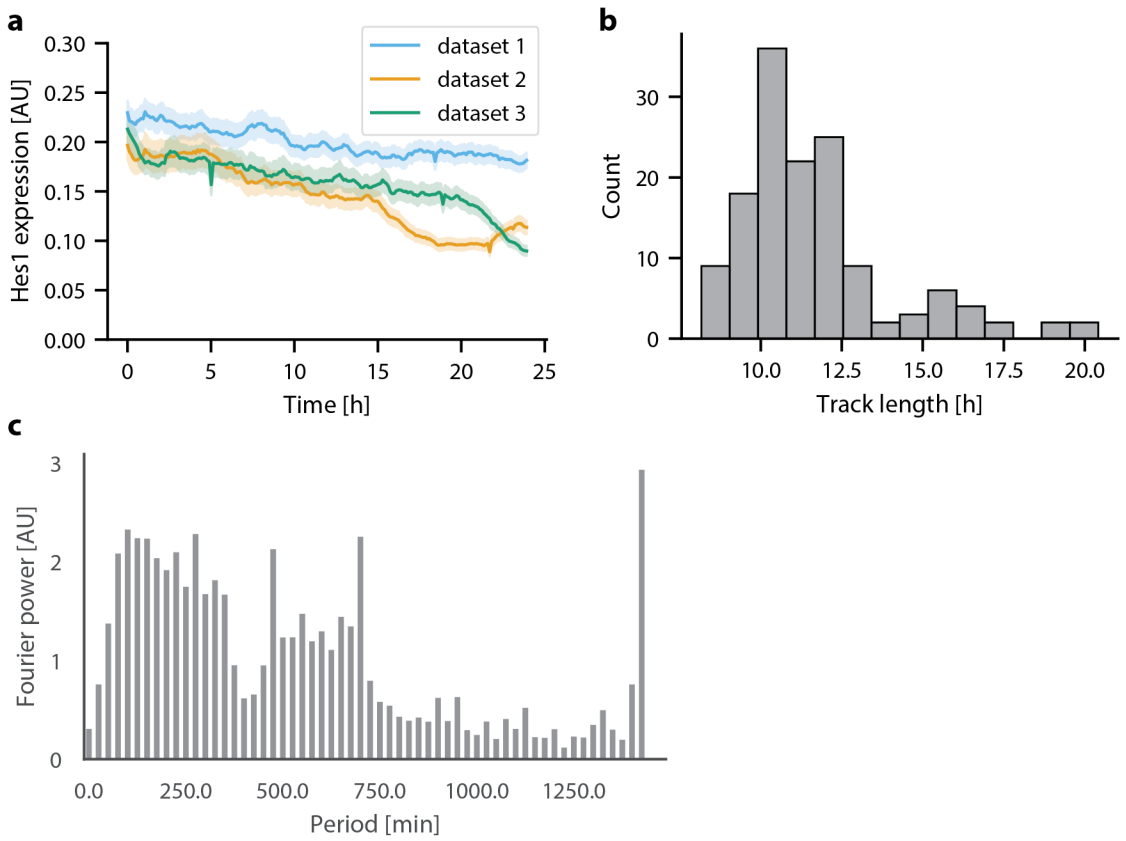

Extended Data Fig. 7. Further analysis of single-cell Hes1-Achilles traces. Intestinal organoids expressing Hes1-Achilles and H2B-mCherry were cultured in 2D, followed by live-imaging and analysis. (a) Plot of Hes1-Achilles intensity vs time for all single-cell tracks, track $n_{dataset1}$ = 2729, $n_{dataset2}$ = 2102, $n_{dataset3}$ = 1705. (b) Histogram of track length from division to division, for all proliferative cells, n = 140. (c) Mean Fourier power spectrum for all single-cell Hes1-Achilles intensity traces, before removing contributions from harmonics related to track length (after removal in Fig. 2b). N=3 biological replicates.

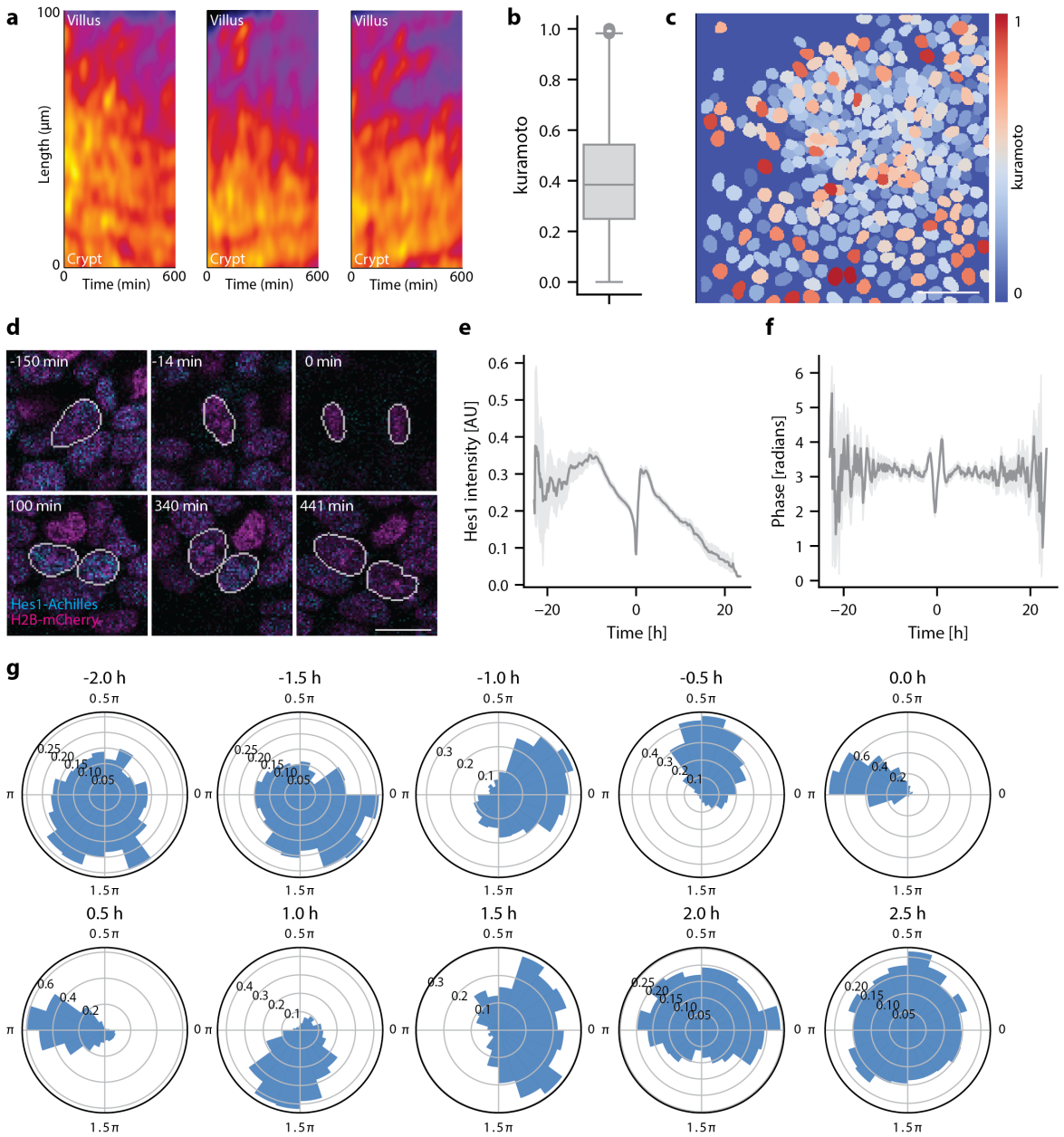

Extended Data Fig. 8. Local synchronisation of Hes1 dynamics. Intestinal organoids expressing Hes1-Achilles and H2B-mCherry were cultured in 2D, followed by live-imaging and analysis. (a) Examples of kymographs taken from timelapse images lines of 2D organoids expressing Hes1-Achilles (see Fig. 2d). (c) Boxplot of Kuramoto order parameter calculated for the direct neighbours of all cells at all timepoints, n_{inst} = 147959 instantaneous measurements. (d) Representative snapshot of segmented nuclei showing Kuramoto order parameter. Scale bar: 50 µm. (e) Representative snapshots of a dividing cell, taken from live imaging of 2D organoids. Scale bar: 5 µm. (f) Hes1-Achilles oscillation phase and (g) intensity vs time for all dividing cells, centred around division, n = 905 tracks. (h) Polar histogram of Hes1-

Achilles oscillation phase at each indicated time around division, radial axis representing count frequency.

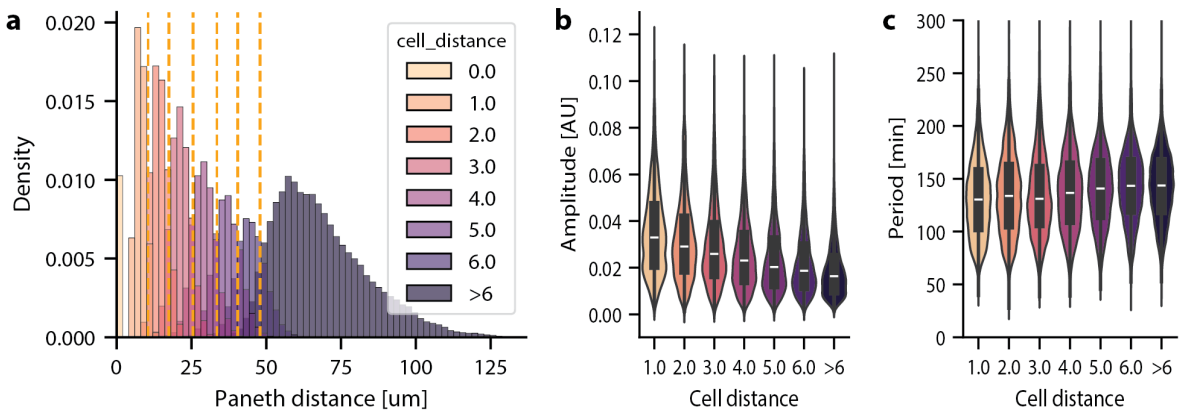

Extended Data Fig. 9. Analysis of single-cell tracks with distance from crypt centre. Intestinal organoids expressing Hes1-Achilles and H2B-mCherry were cultured in 2D, followed by live-imaging and analysis. (a) Histogram showing the distribution of cells from Paneth cells, n = 308156 cells for all timepoints. (b) Violin plot of amplitude vs distance from Paneth cells. (c) Violin plot of period vs distance from Paneth cells. n=1901 tracks, N=3 biological replicates, n_{inst} = 147959 instantaneous measurements. Normal distribution was assessed by Shapiro Wilk test, $p<0.05$ for all datasets. Significance was tested by Mann-Whitney U test, with all other cell distances compared against cell distance = 1. All comparisons were statistically significant, $p<0.05$.

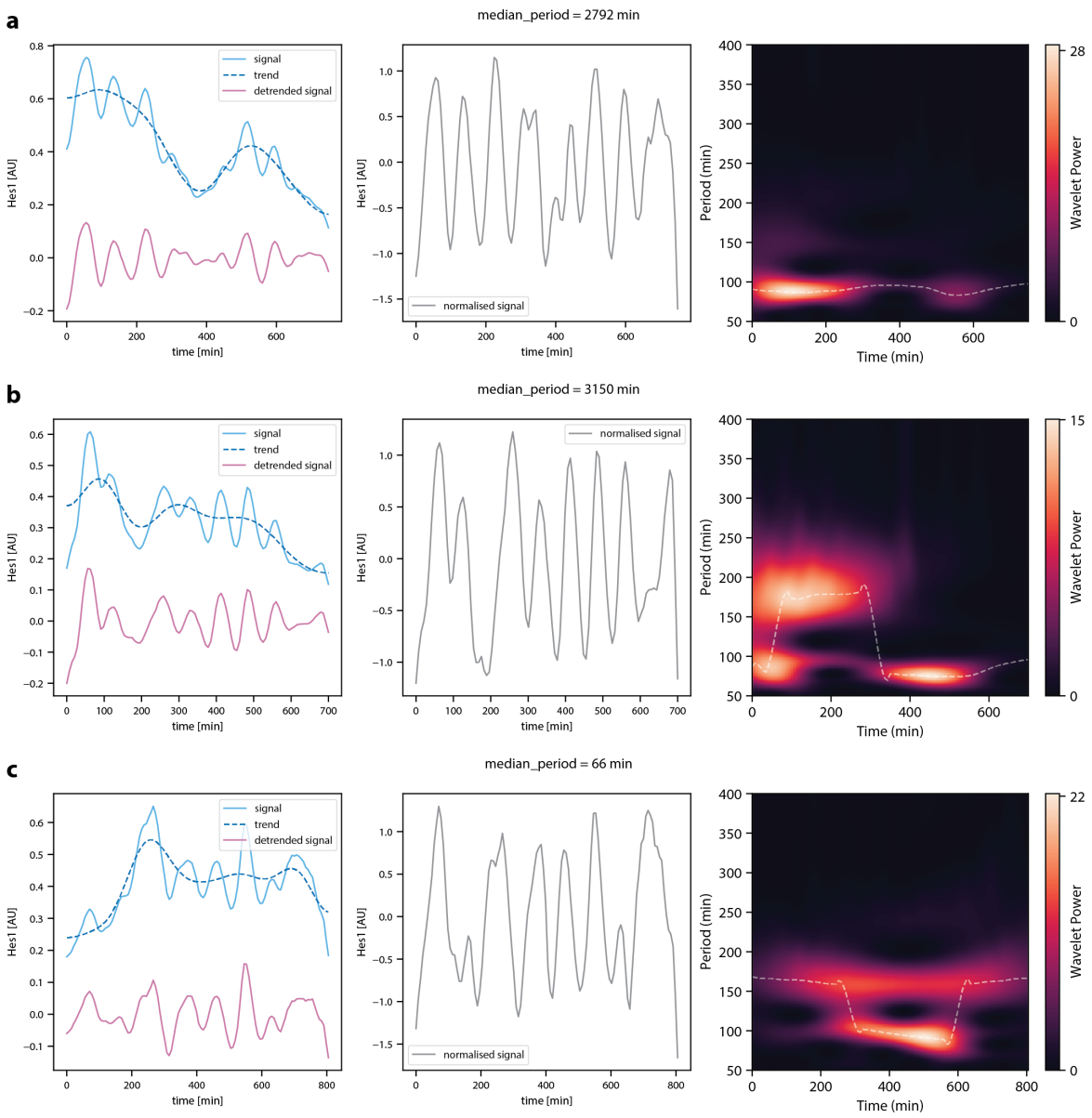

Extended Data Fig. 10. Examples of wavelet power spectra. Intestinal organoids expressing Hes1-Achilles and H2B-mCherry were cultured in 2D, followed by live-imaging and analysis. (left) Time traces of smoothed (original) Hes1-Achilles intensity signal, trend line and detrended signal. (centre) Time trace of amplitude normalised Hes1-Achilles signal. (right) Wavelet power spectra calculated from amplitude normalised Hes1-Achilles signal.

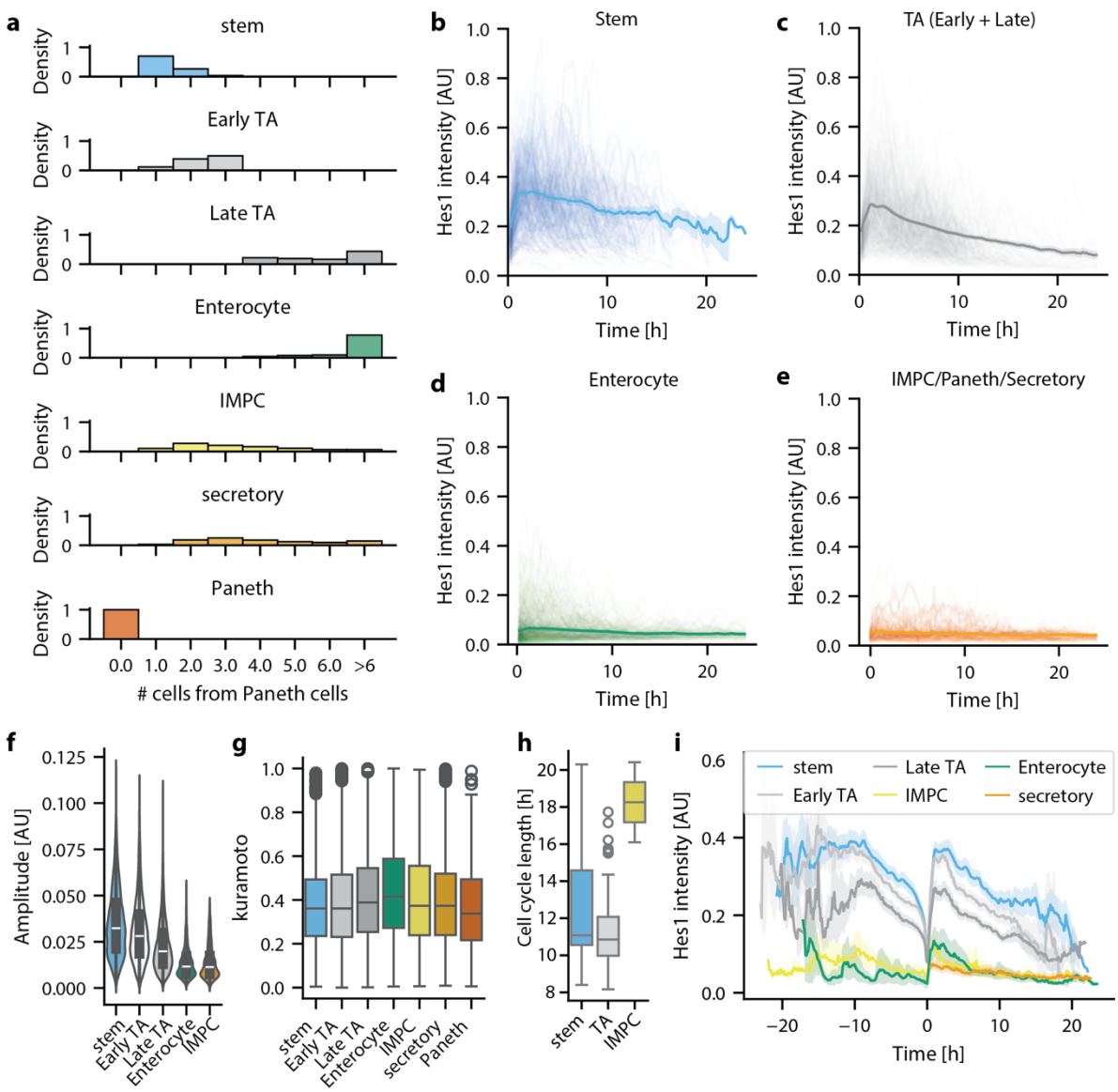

Extended Data Fig. 11. Further analysis of cell-type specific Hes1 dynamics. Intestinal organoids expressing Hes1-Achilles and H2B-mCherry were cultured in 2D, followed by live-imaging and analysis. (a) Histogram showing distribution of distances of different cell types from Paneth cells, n = 308156. (b-e) Hes1-Achilles intensity vs time for different cell types, n= 1901 tracks. (f) Violin plot of amplitude vs cell type. (g) Boxplot of Kuramoto order parameter per cell type. For (b-g), n = 1901 tracks. (h) Boxplot of cell cycle length per cell type, n = 182 tracks. (i) Hes1-Achilles intensity vs time for all dividing cells per cell type, centred around division, n = 905 tracks.

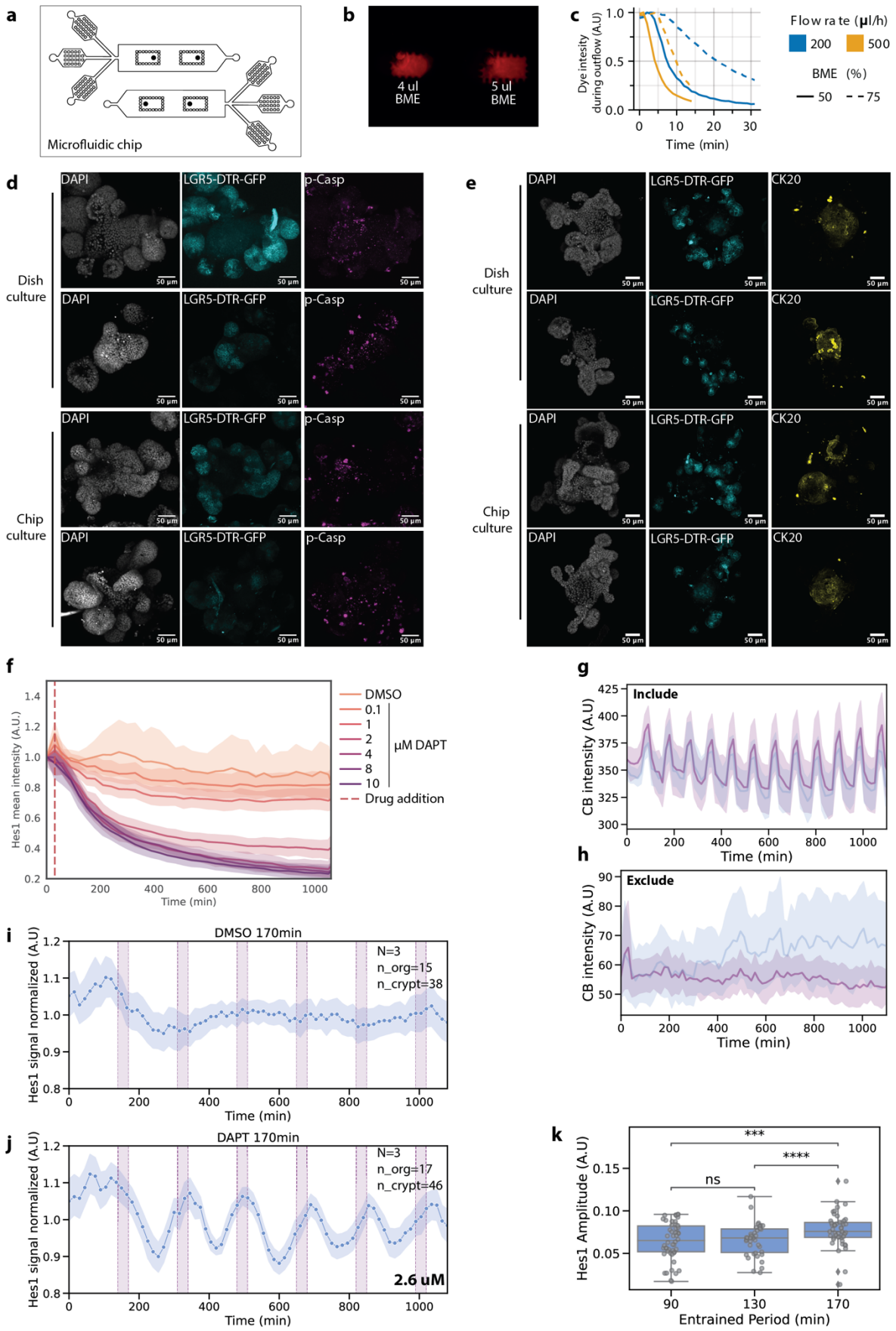
a
Microfluidic chip
b
4 ul BME
5 ul BME
c
Dye intesity during outflow (A.U)
Time (min)
Flow ra te (µl/h)
200
500
BME (%)
50
75
d
Dish culture
Chip culture
DAPI
LGR5-DTR-GFP
p-Casp
50 µm
e
Dish culture
Chip culture
DAPI
LGR5-DTR-GFP
CK20
50 µm
f
Hes1 mean intensity (A.U.)
Time (min)
DMSO
0.1
1
2
4
8
10
µM DAPT
Drug addition
g
Include
CB intensity (A.U)
Time (min)
h
Exclude
CB intensity (A.U)
Time (min)
i
DMSO 170min
N=3
n_org=15
n_crypt=38
Hes1 signal normalized (A.U)
Time (min)
j
DAPT 170min
N=3
n_org=17
n_crypt=46
2.6 uM
Hes1 signal normalized (A.U)
Time (min)
k
***
****
ns
Hes1 Amplitude (A.U)
Entrained Period (min)

1247

Extended Data Fig. 12. Optimization of modulating oscillations in intestinal organoids on microfluidic chips. (a) Schematic representation of chip design, two separate chambers for control (DMSO) and test (DAPT) conditions. Two organoid loading sides, three inlets and one outlet per condition. (b) Optimization of BME loading amount, fluorescent dye was added to BME. 4µl stayed within the bubble traps whereas 5µl spread through the chip (c) Dye intensity over time when following outflow of the chip. Graph indicates optimization of flow-rate and BME concentration, 200µl/h and 50% BME were chosen for the following experiments. (d) Representative images of organoids cultured on a dish versus organoids cultured on a microfluidic chip. LGR5-DRT-eGFP organoids were stained for phospho-Caspase, an apoptosis marker, and counterstained with DAPI. (e) Representative images of organoids cultured on a dish versus organoids cultured on a microfluidic chip. LGR5-DRT-eGFP organoids were stained for CK20, an enterocyte marker, and counterstained with DAPI. (f) DAPT titration from 0.1uM-10uM, on Hes1-Achilles organoids. Hes1-Achilles intensity was detected over time per crypt and normalized to the first timepoint (untreaded). Red dotted line represents treatment start time of 30 min. N=3, n_organoid= 9, n_crypt = 33 +/-3.7. (g-h) Representation of Caspase Blue (CB) intensity over time for two different microfluidic experiments. (g) Experiments that were included, (h) experiments that were excluded. (i) Entrainment of Hes1-Achilles oscillations to periodic pulses of 170-min of the NOTCH inhibitor DAPT (concentration indicated). Quantification of (normalized) Hes1-Achilles signal in organoid crypts. Experiments (N = independent experiments, n_org = individual organoids, n_crypt = individual crypts) were combined using the external force (pink bars) as an objective time reference. (j) Quantification of amplitude by wavelet transform and comparison between entrainment periods with following DAPT conditions; 90min = 1.38µM DAPT, 130min = 2µM DAPT, 170min = 2.6µM DAPT. Normal distribution was calculated by Shapiro Wilk test and significance was tested by independent t-test or Mann-Whitney U test depending on normal distribution and Bonferroni correction was performed to take multiple samples into account. ns: 5.00e-02 < p <= 1.00e+00, *: 1.00e-02 < p <= 5.00e-02, **: 1.00e-03 < p <= 1.00e-02, ***: 1.00e-04 < p <= 1.00e-03, ****: p <= 1.00e-04.

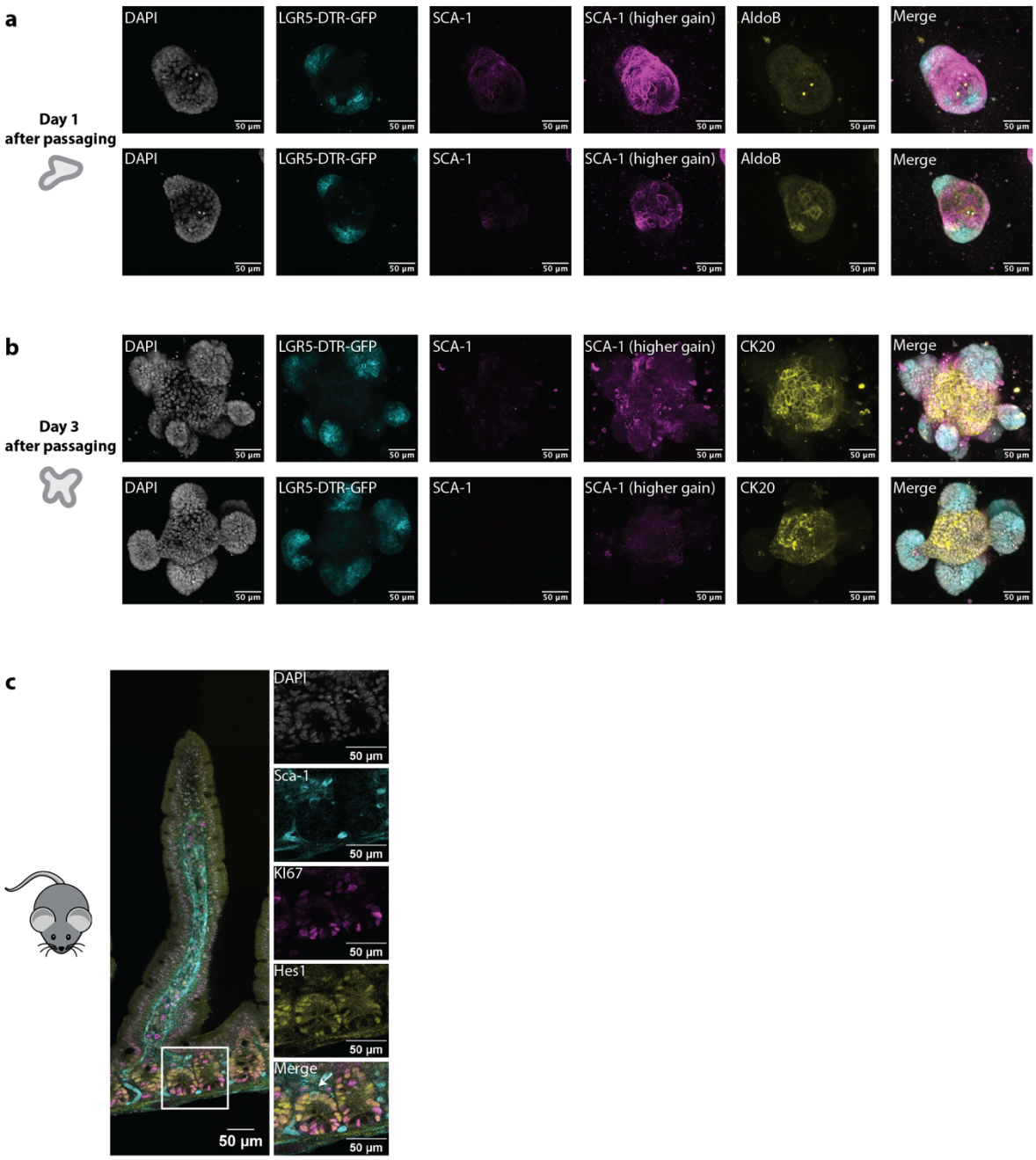

Extended Data Fig. 13 Organoid size and cell composition after passaging showing the fetal-like stem cell marker SCA. (a, b) Representative maximum intensity images of organoids 1 day (a) or 3 days (b) after passaging. LGR5-DTR-GFP organoids were stained for a fetal-like stem cell marker, SCA-1, enterocyte marker AldoB or CK20 and counterstained with DAPI. SCA-1 was depicted with a low and high threshold based on low, but present SCA-1 intensities at 3 days after passaging. (c) Representative image of Hes1-Achilles gut-slices, stained with a proliferation marker KI67, fetal-like stem cell marker, SCA-1, and counterstained with DAPI. Magnification of the crypt is shown and SCA-1 positive cell is indicated by an arrow.

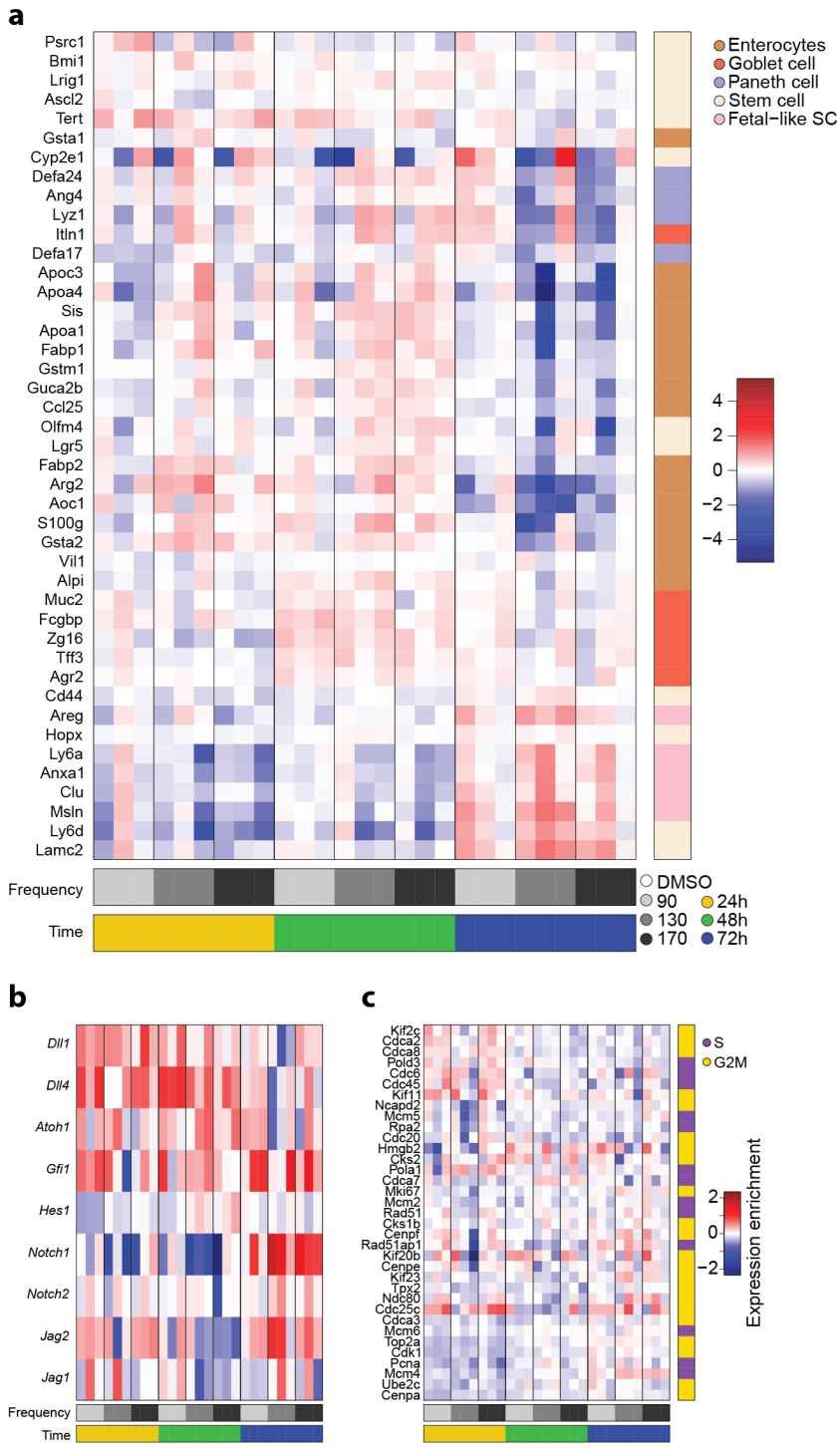

Extended Data Fig. 14. Analysis of bulk RNAseq data after entraining to different periods and durations. Hierarchical clustering of gene expression profiles of cell type specific genes (a) gene expression correlation profiles related to the NOTCH pathway (b) or to cell cycle activity (c), subdivided by entrainment and duration of entrainment. Z-score is shown. Values represent fold change relative to time-matched DMSO controls.

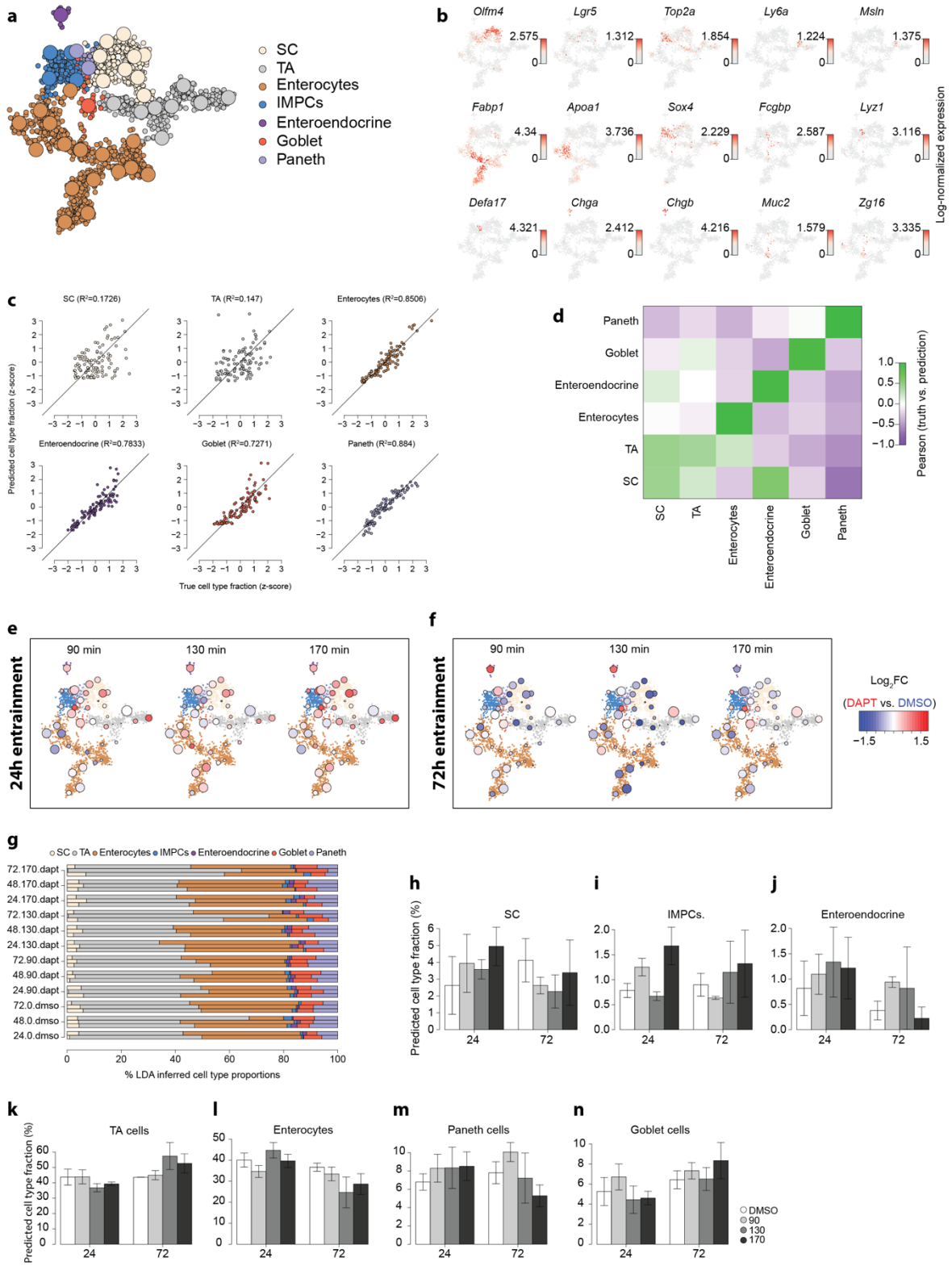

Extended Data Fig. 15. Effect of entrainment on intestinal organoids analysed by bulk RNA sequencing and Latent Dirichlet Allocation (LDA) analysis. (a) Clustering re-analysis of single-cell RNAseq data presented in Bues et al.,2022[40]. Dots represent single cells and circles represent metacells[60]. Cells and metacells are

1301 coloured by assignment to cell types. (b) Expression of lineage markers across the
1302 reanalyzed single-cell RNAseq data as in (a). Dot color indicates log normalized
1303 expression. (c, d) Validation of LDA predictions across datasets and sequencing
1304 platforms. Single-cell RNAseq data from Haber et al. (2017)[12] was projected on the
1305 data from Bues et al. (2022)[40]. Then 100 pseudo-bulk aggregates of 200 cells each
1306 were generated and analysed via the LDA pipeline (see Methods for further details).
1307 (c) Predicted cell type proportions (z-score; *y* axis) are plotted against their true value
1308 per aggregate (z-score, *x* axis). R2 values are indicated per cell type. (d) Pearson
1309 correlation values between predicted and true cell type proportions are shown. (e, f)
1310 Results of the LDA deconvolution of the 24h (e) or 72h (f) bulk RNAseq data on top of
1311 the single-cell clustering analysis as in (a). Metacells are coloured by fold-change in
1312 their predicted proportions compared to the time-matched DMSO controls. (g)
1313 Predicted cell type distributions for each sample included in the bulk RNAseq data,
1314 based on the LDA analysis. (h-n) Predicted percentage of stem cells (h), secretory
1315 progenitors (i), enteroendocrine cells (j), TA cells (k), Enterocytes (l), Paneth cells (m)
1316 and Goblet cells (n) per entrainment vs control (DMSO) per experimental duration
1317 including 24 and 72 hours, based on the LDA analysis.

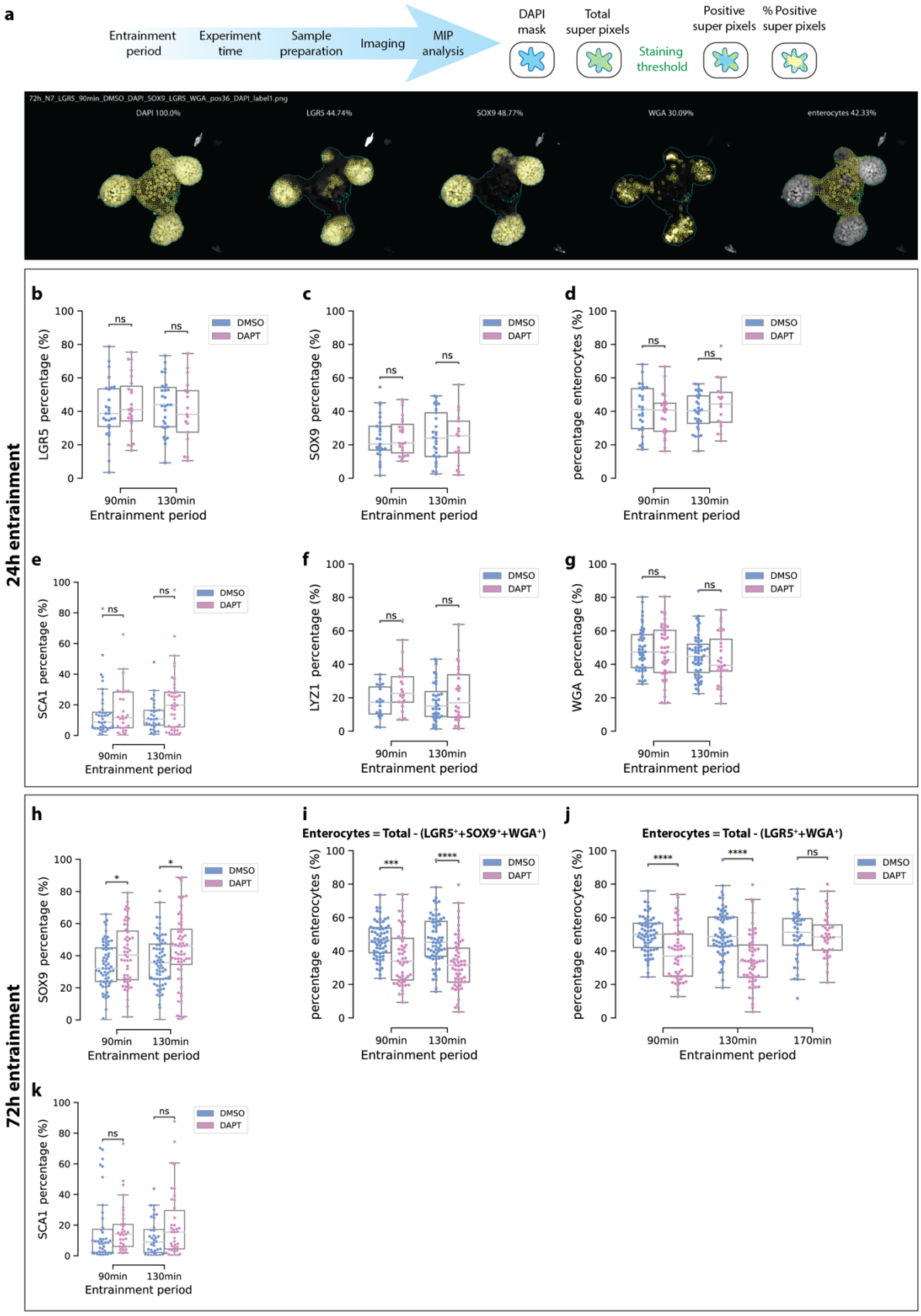

Extended Data Fig. 16. Cell type composition of intestinal organoids after entrainment. (a) *Upper panel:* Schematic representation of experiments, sample

processing and image analysis. *Lower panel:* Representative images of DAPI mask and superpixel calculation. (b-g) Quantitative analysis of cell percentage per organoid compared to control (DMSO) for 90-,130-min entrainment for 24 h. Cell percentages tested for LGR5 (b), SOX9 (c), Enterocytes (d), SCA-1 (e), LYZ1 (f), WGA(g). (h-k) Quantitative analysis of cell percentage per organoid compared to control (DMSO) for 90-,130- (h, i, k) and 170-min (j) entrainment for 72 h and representative images including percentage. Cell percentages tested for SOX9 (h), Enterocytes (I, j), SCA-1 (k). Enterocytes in (j) were calculated without SOX9, so 170-min entrainment could be included. N= minimum of 3 and n_org = minimum of 14 organoids per condition. Normal distribution was calculated by Shapiro Wilk test and significance was tested by independent t-test or Mann-Whitney U test depending on normal distribution. ns: 5.00e-02 < p <= 1.00e+00, *: 1.00e-02 < p <= 5.00e-02, **: 1.00e-03 < p <= 1.00e-02, ***: 1.00e-04 < p <= 1.00e-03, ****: p <= 1.00e-04.

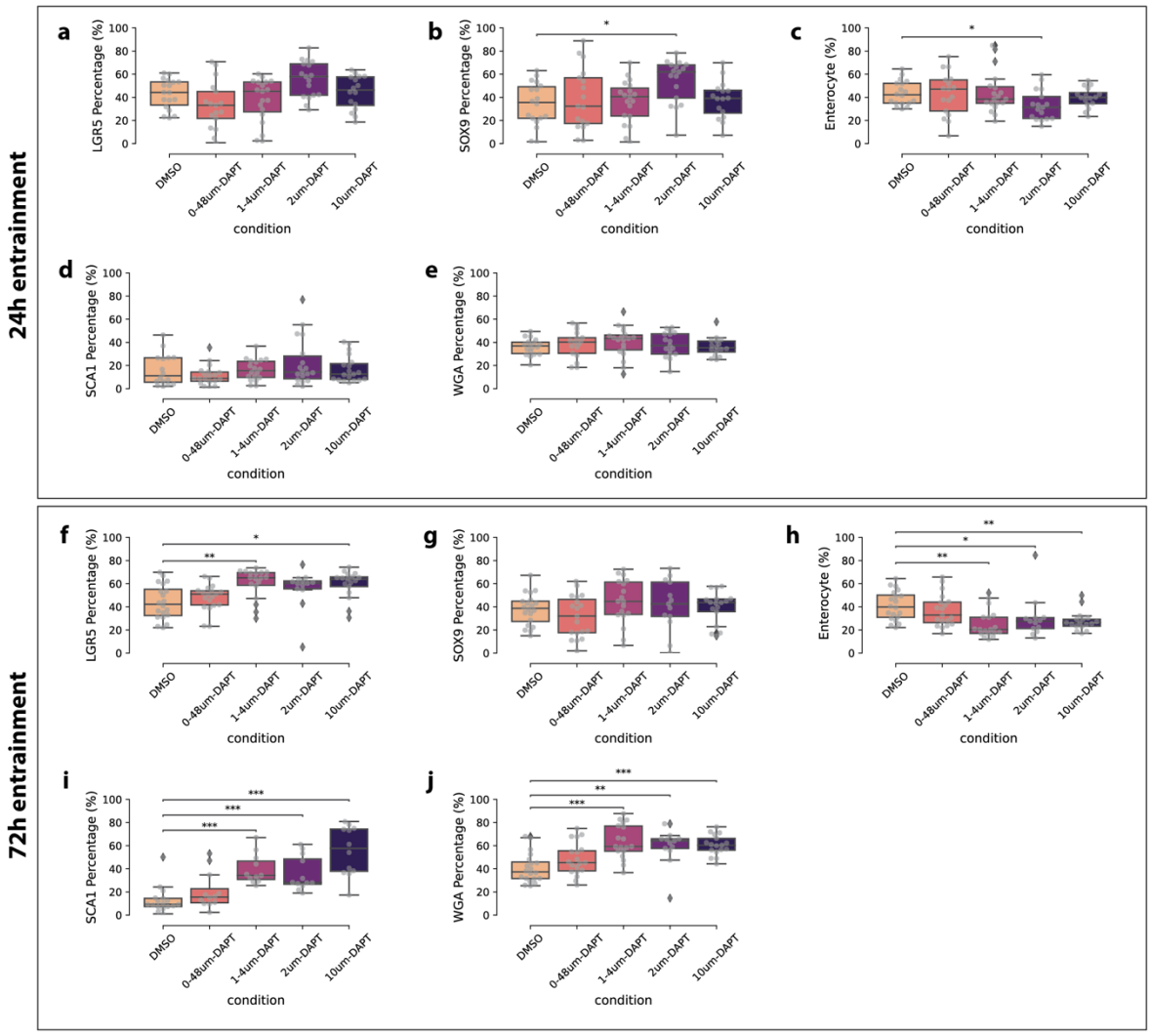

Extended Data Fig. 17. Cell type composition after constant DAPT treatment. Quantification of cell percentage per organoid by superpixel analysis when organoids are treated with 0,48μM, 1.4μM, 2μM and 10μM compared to control (DMSO) for a period of 24 hours (a-e) or 72 hours (f-j). Organoids were treated the same as the microfluidic experiments, passaged 1 day before a 72 h experiment and 3 days before a 24 h experiment. LGR5-DTR-GFP (a, f) or WT organoids were used and stained for SOX9 (b, g) a proliferation marker. Enterocytes were calculated by total superpixels – (LGR5+SOX9+WGA superpixels) (c, h). Organoids were stained for SCA-1 (d, i) a fetal-like stem cell marker or WGA (e-j) a secretory cell type marker. Normal distribution was calculated by Shapiro Wilk test and significance was tested by independent t-test or Mann-Whitney U test depending on normal distribution. Due to multiple samples Bonferroni correction was performed. ns: 5.00e-02 < p <= 1.00e+00,

*: 1.00e-02 < p <= 5.00e-02, **: 1.00e-03 < p <= 1.00e-02, ***: 1.00e-04 < p <= 1.00e-03, ****: p <= 1.00e-04.

1352 **Supplementary Table 1: Genotype Primers**

Construct	Fw 5'- 3'	Rv 5'- 3'
Rosa_H2B_mCherry	GCTTCAAGGTGCACATGGAG	CATGAACTGAGGGGACAGGA
WT_Rosa_locus	CGTGATCTGCAACTCCAGTC	GGAGCGGGAGAAATGGATATG
Hes1_Achilles	GACCTCGGTGGGTCCTAACGC	CTTGCCGGTGGTGCAGATCAG
WT_Hes1	GACCTCGGTGGGTCCTAACGC	GAGGTGGGCTAGGGACTTTACGG
Nucmem_IRFP	GAGCTGCAGTGGAGTAGGCG	CTCGACCATGGTAATAGCGA

1353

1354

1355 **Supplementary Table 2: Antibodies**

Target	concentration	Fixation time (min)	Host Species	Article number
Ki67	1:200	10-45 (3D)	Rat	14-5698-82 (ebioscience)
Ki67	1:200	10-45 (3D)	Rabbit	ab16667
Lyz1	1:200	45 (3D)	Rabbit	A0099 (DAKO)
CK20	1:200	10 (3D)	Mouse	M701929-2 (DAKO)
WGA	1:500	45 (3D)	-	29026-1 (Biotium)
Sox9	1:200	45 (3D)	Rabbit	ab185966
Olmf4	1:200	20	Rabbit	39141 (XP)
Hes1	1:200	5 (3D)	Mouse	sc-166410
Cleaved Caspase-3	1:200		Rabbit	9661S(cell signaling tech.)
AldolaseB	1:200	10 (3D)	Rabbit	ab75751
Muc2	1:200	20	Rabbit	NBP1-31231
ChrA	1:200	45	Mouse	sc-13090
Sca-1	1:300	10 (3D)	Rat	Ab51317

1356

1357

1358

1359 **Supplemental movies**

1360 **Supplemental movie 1. Intravital Imaging following a single cell.** Cyan: H2B-
1361 mCherry, purple: Hes1-Achilles.

1362 **Supplemental movie 2. Light-Sheet imaging of 3D organoid expressing Hes1-**
1363 **Achilles.**

1364 **Supplemental movie 3. Imaging of 2D culture of intestinal organoids.** Purple:
1365 H2B-mCherry, cyan: Hes1-Achilles.

1366 **Supplemental movie 4. Segmentation of 2D culture movies.** Purple: H2B-mCherry,
1367 cyan: Hes1-Achilles.

1368 **Supplemental movie 5. Tracked single cell in 2D culture.** Purple: H2B-mCherry,
1369 cyan: Hes1-Achilles.

1370 **Supplemental movie 6. Quantification of synchronization using Kuramoto order**
1371 **parameter.** *Left panel*: Cells labelled according to their Kuramoto order parameter
1372 (blue = 0, red = 1); *Middle panel*: Hes1-Achilles; *Right panel*: H2B-mCherry.

1373 **Supplemental movie 7. Track of a dividing cell.**

1374 **Supplemental movie 8. TA cell to enterocyte differentiation.**

1375 **Supplemental movie 9. Stem cell to IMPC differentiation.**

1376 **Supplemental movie 10. Imaging of organoids expressing Hes1-Achilles in**
1377 **microfluidic chip.** Entrainment using 130 min drug pulses. *Left panel*: DMSO control;
1378 *Right panel*: DAPT.

1379

1380